Master Thesis

Electronic Raman spectroscopy of metallic carbon nanotubes

(金属カーボンナノチューブの電子ラマン分光)

Department of Physics

Graduate School of Science, Tohoku University

Eddwi Hesky Hasdeo

2013

Acknowledgements

I thank Prof. R. Saito for his guidence through two years of my master course. I am very thankful for his supportive spirit to keep me move forward to the goal. A. R. T. Nugraha has been the best tutor for me not only in doing physics but also in developing my skill of pingpong, traditional music, writing, and many more. He has become my long-life brother. Dr. K. Sato, has been teaching me and lend me many books so that I can understand the basic physics of carbon nanotube, Raman spectra, and a lot more. I also want to give my gratitude to Dr. W. Izumida for his stimulating discussion, especially during calculation of the electron-electron interaction. For my lab mates and ex-lab mates, Tareque, Tapsanit, Tatsumi, Thomas, Mizuno, and Ominato, thank you very much for the time we spend together during book reading, it was very fun and challenging as well. I thank to Prof. Millie Dresselhaus from MIT, for her important support during the writing of my paper. I acknowledge the financial support from MEXT during my master course. Last but not least, I give my deep awe to my heroes, papa and mama, for their pray and faith to make their son to be as what he is now.

Contents

Chapter 1

Introduction

1.1 Purpose of the study

A single wall carbon nanotube (SWNT) is a single-layer graphite sheet rolled up into a cylinder, with diameter $\sim$1 nm and length $\sim$1 μm. In comparison with its length, a SWNT diameter is small enough, thus a SWNT can be regarded as a quasi one-dimensional (1D) material. Depending on how we roll up the graphene sheet, the geometry of SWNT is defined by a chirality index (n, m). The (n, m) value determines whether a SWNT is metallic (m-SWNT) or semiconducting (s-SWNT). In m-SWNTs, the existence of the gapless linear energy band in m-SWNT provides an interesting phenomenon of a 1D electron [1]. In this thesis, we discuss the origin of so-called electronic Raman spectra as shown below observed only in m-SWNTs.

Raman spectroscopy is a technique to study optical properties of a material based on the inelastic scattering of light. In SWNTs, Raman spectroscopy generally provides a decent understanding of phonons excitation. For instance, the radial breathing mode (RBM), an atomic vibration mode along the radial direction, appears in Raman spectra at $50 \sim 200$ cm^{-1} and a longitudinal optic (LO) mode together with an in-plane transverse optic (iTO) mode form the G band Raman spectra around $1550 - 1570$ cm^{-1}.

One method for distinguishing s-SWNTs from m-SWNTs is based on the distinct feature of the G band. The G band feature of s-SWNTs shows the symmetric Lorentzian lineshape, while that of m-SWNTs shows the asymmetric Breit-Wigner-Fano (BWF) lineshapes [2].

The BWF line shape, which is a general physical phenomenon, comes from the interference between the continuum spectra with the discrete spectra [3]. In m-SWNTs, the discrete spectra comes from phonon excitations, and the continuum spectra comes from electron excitations. The existence of a gapless linear energy band (Dirac cone) in m-SWNTs modifies the symmetric G band spectra to give an asymmetric lineshape. Observations of electronic contribution to the Raman spectra had been noticed since last decade [4, 5, 2], however the apparent clarification towards this spectra has been accomplished by Farhat et al [6]. He observed a broad spectrum with well-defined peak only in m-SWNTs and no such feature in s-SWNTs. This spectrum is ascribed to the electronic Raman scattering (ERS) since this spectra originate from pure electron excitation. However, our understanding of the electronic spectra remains unclear since there is no theoretical work that successfully reproduced the Raman spectra of m-SWNTs from the experimental data.

The purpose of this thesis is to provide a conclusive theoretical description of the ERS mechanism. Based on gate-modulated Raman spectroscopy (Sec. 1.2.3 and 1.2.4), the origin of ERS comes from a single particle (electron-hole) excitation within the linear energy band of m-SWNTs by means of the Coulomb interaction. The Coulomb interaction describing the interaction between the photo-excited carrier and the electron-hole pairs in the linear band is introduced within exciton-exciton matrix elements. Our calculation is performed under the extended tight binding method (ETB) for electronic structures and exciton wave functions. The Coulomb potential is modeled by the Ohno potential which gives the effective potential for π electron interaction in sp^2 carbon systems. From this calculation, we found that the first-order ERS process vanished for $\mathbf{q} = 0$ momentum though the Coulomb interaction as a function of $\mathbf{q}$ reach a maximum at $\mathbf{q} = 0$ (Sec. 3.3). We argue that the vanishing Coulomb interaction at $\mathbf{q} = 0$ is due to the symmetry of sublattice wave function. By considering the second-order process with $\mathbf{q} \neq 0$, we can reproduce the Raman spectra consistent with the experimental data (Sec. 4.2). Furthermore, we show that the BWF feature of m-SWNTs comes from the interference between the G band and the ERS spectra. We also demonstrate how the asymmetry, spectral width, and peak position of the G band might be affected by the ERS as a function of laser excitation energy. Finally, based on this theory we predict that the radial breathing mode (RBM) spectrum should show the BWF line shape as well.

We expect that this work will also give clarifications for presently available experimental results and insights for future experimental studies.

This master thesis is organized as follows: In the remaining part of Chapter 1, the background for understanding this thesis is given. In Chapter 2, the electronic and excitonic properties of SWNTs is reviewed. In Chapter 3, we will show our original result of exciton-exciton matrix elements calculation which later contributes to the ERS spectra. We will present the detail of calculation in the TB method and show the vanishing of matrix elements at $\mathbf{q} = 0$. In Chapter 4 we compare our calculated result of the ERS spectra with the experimental data. We will analyze the asymmetry of both the G band and RBM by fitting to the BWF lineshape. The asymmetry factor $1/q_{\mathrm{BWF}}$, the spectral width, and the peak position of the G band and RBM will be analyzed as a function of E_{L}.

1.2 Background

Here we show the background concepts which are important to this thesis.

1.2.1 Raman Spectroscopy in SWNTs

One technique to study the optical properties of SWNTs is Raman spectroscopy. Raman spectroscopy is an inelastic scattering of light, in which the outgoing light energy differs from the incoming energy. The energy shift the scattering process originates from different kinds of elementary excitations, for example: atomic vibrations (phonons), electron excitations (excitons), charge density waves (plasmons), and spin density waves (magnons). Study of Raman spectroscopy in SWNTs reveals that the phonon gives the dominant contribution for the observed Raman spectra. A positive (negative) shift energy of the scattered light corresponds to absorption (emission) of phonons, which is called an anti-Stokes (Stokes) Raman scattering. The conventional unit for Raman shift energy is cm^{-1} ($1\ \mathrm{eV} = 8065\ \mathrm{cm}^{-1}$).

Phonon excitations may occur in the first-order or higher-order Raman processes. The first-order Raman process is defined by one phonon emission during a scattering event. The higher-order process incorporates overtones or combinations of the phonon modes within one scattering event. The atomic vibration along the tube radial direction, also known as,

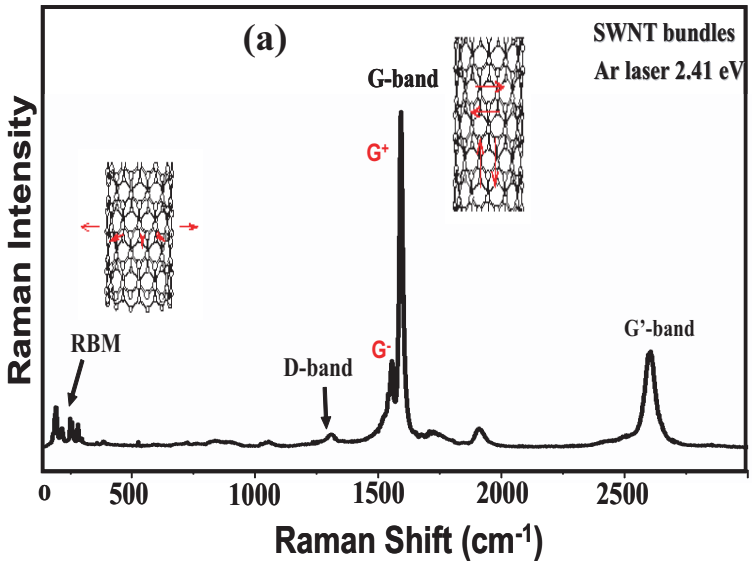

Figure 1-1: Raman spectra taken from high pressure carbon monoxide (HiPCO) SWNT bundle with a excitation laser energy at 2.41 eV. The spectra show the radial breathing mode (RBM) at $50 \sim 200$ cm^{-1}, D band (~ 1350 cm^{-1}), G band ($1550 - 1570$ cm^{-1}), and G$'$ band (2700 cm^{-1}) features [10].

radial breathing mode (RBM), vibration along the tube axis, Longitudinal optic mode (LO), and vibration along the tangential direction, in-plane transverse optic mode (iTO) are the examples of the first-order Raman process [7] (Fig. 1-1). The LO and iTO modes constitute the G mode which are degenerated in case of graphite but are splitted into two peaks, i.e. G^+ and G^- in case of SWNT due to the curvature effect [8]. The G$'$ band is a second-order order Raman process which is assigned as the overtone of iTO phonon mode around the K point, hexagonal corner of graphene Brillouin zone [9]. The D band phonon mode comes from the defect.

If we look very closely at the G band in s-SWNTs and m-SWNTs, we may observe distinct features at those spectra (Fig. 1-2). In a m-SWNT, the G band shows somewhat a broad asymmetric lineshape while in a s-SWNT is symmetric. This asymmetry in m-SWNT occurs due to a electronic excitation around the metallic band whose spectrum interferes with the G band phonon mode. The symmetric (asymmetric) lineshape in s-SWNTs (m-SWNTs) are generally fitted by Lorentzian (Breit-Wigner-Fano) formula. The Breit-Wigner-Fano (BWF)

Fig. 1-1: fig/intro-raswnt1.eps

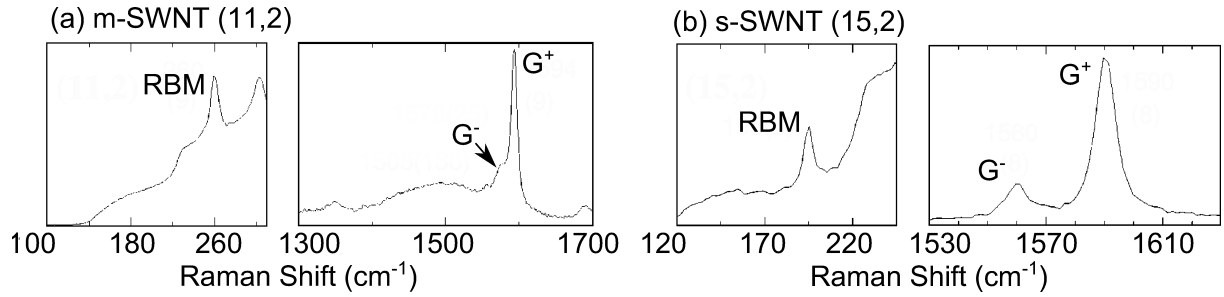

Figure 1-2: The RBM, G^+, and G^- Raman spectra for (a) (11,2) m-SWNT and (b) (15,2) s-SWNT [12]

lineshape appears in many metallic systems which posses electronic spectra (Sec. 1.2.5). The electronic structure for s-SWNTs and m-SWNTs will be discussed in Section 2.1.

1.2.2 Resonance Raman spectroscopy

Intensity of the scattered light in Raman spectroscopy is generally very weak; however, when the laser energy is resonant to the separation energy between the conduction and valence bands, the intensity is strongly enhanced which we call resonance Raman effect. In one dimensional (1D) material like SWNTs, the transition energy between valence and conduction band can be clearly defined due to singularities of 1D density of states, known as, Van Hove singularities (VHS). Between two VHS in the ith valence band and the ith conduction band, the transition energy is labeled by E_{ii}, which depends on the geometry of SWNTs [11]. Therefore matching the laser excitation energy E_{L} to E_{ii} will provide Raman spectra for given SWNTs (n, m) value [8], thus giving information of the E_{ii} for (n, m) SWNT. This is called resonance Raman spectroscopy (RRS).

For characterization purposes, the RBM is particularly of great importance since it is directly related to the nanotube diameter d_t [13]. Its frequency, ω_{RBM}, depends on d_t and can be estimated by $\omega_{\mathrm{RBM}} = A/d_t + B$, where $A = (227.0 \pm 0.3)$ cm^{-1}nm and $B = (0.3 \pm 0.2)$ cm^{-1}for supergrowth sample [14]. These parameters are sensitive to environment. This relation is very useful for extracting the nanotube diameter from the RBM position. A typical RBM range is about $100 - 350$ cm^{-1}.

Fig. 1-2: fig/intro-ms-swnt.eps

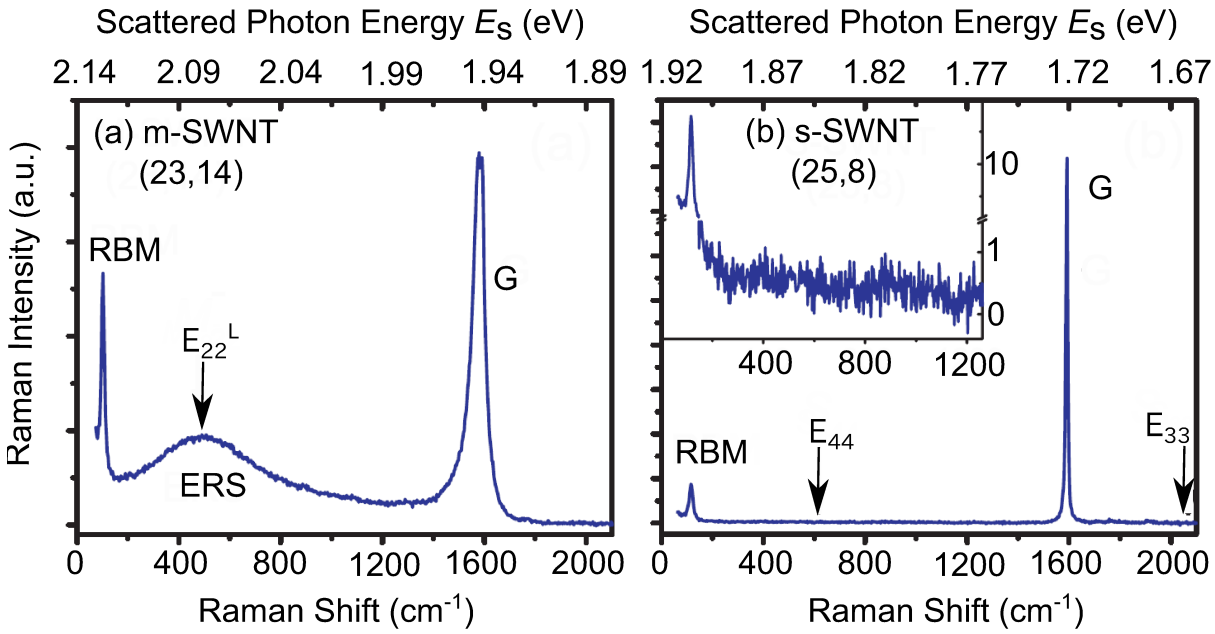

Figure 1-3: (a) the ERS feature is observed at optical transition energy E_{22}^{L} in a (23,14) m-SWNT. (b) no ERS feature in a (25,8) s-SWNT [6]

1.2.3 Electronic Raman scattering in m-SWNTs

The unambiguous observation of the electronic contribution toward an inelastic scattering of light in m-SWNTs has been done by Brown et al. [2]. They observe that G^- is asymmetric in m-SWNTs. The spectra are nicely fit to BWF formula and their asymmetric factor is proportional to inverse diameter of m-SWNTs. Farhat et al. [6] later observed an exclusive feature found only in m-SWNTs (Fig. 1-3a) but not in s-SWNTs (Fig. 1-3b) and assigned the spectrum as the electronic Raman scattering (ERS). The ERS spectra with a peak located at transition energy E_{22}^{L} gives a very broad ($\sim$500 cm^{-1}) shape, as what we expect for continuum scattering, and appears between the RBM and the G bands with shift energy around 0.06 eV. Because of the ERS broad feature, the G band and RBM lineshapes become asymmetric in m-SWNTs.

Figure 1-4(a) shows the experimental result of E_{L} dependence of Raman spectra. The spectra show that the phonons' peak positions shift according to the shift of E_{L} by $E_{\mathrm{L}} - \hbar\omega_{\mathrm{ph}}$ (the phonon energy) while the ERS peak remains at transition energy E_{ii} due to the maxima

Fig. 1-3: fig/intro-ersfarhat.eps

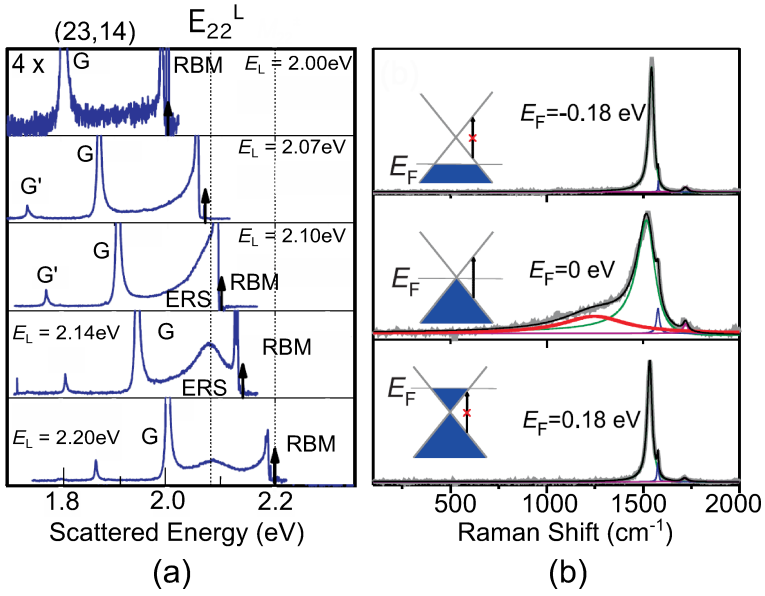

Figure 1-4: (a) E_{L} dependence of the ERS for a $(23, 14)$ m-SWNT. The ERS peak position remains at E_{22}^{L} while the phonons peak are shifted as a function of E_{L}. (b) E_{F} dependence of the ERS. The ERS, shown by the red line, is suppressed when E_{F} is shifted to negative or positive value. E_{F} is changed by applying a gate voltage through the m-SWNT [6].

of the DOS. This distinct behavior indicates that the origin of ERS is not a phonon excitation. Furthermore, by shifting the Fermi energy (E_{F}) to the positive (negative) value from the Dirac cone, the ERS is suppressed (Fig. 1-4 (b)) because of the final (initial) state is occupied (unoccupied). This ERS suppression indicates that the ERS comes from the single-particle electron-hole pairs excitation within the linear band.

1.2.4 Gate-modulated Raman spectroscopy

One technique to enrich the understanding of Raman spectroscopy in m-SWNTs is gate-modulated Raman spectroscopy (GRS). The GRS is used to probe the low-lying electron-hole pairs excitation within the linear energy band of m-SWNTs by applying a gate voltage to the m-SWNTs being studied. E_{F} thus is shifted to a positive or negative value depending on the gate voltage applied (Fig. 1-5(a)).

The GRS is very useful to observe the Kohn anomaly phenomenon in m-SWNTs (Fig. 1-5(b) and (c)) [15], i. e. the shift of phonon energy due to interaction between a phonon and

Fig. 1-4: fig/intro-erselfermi.eps

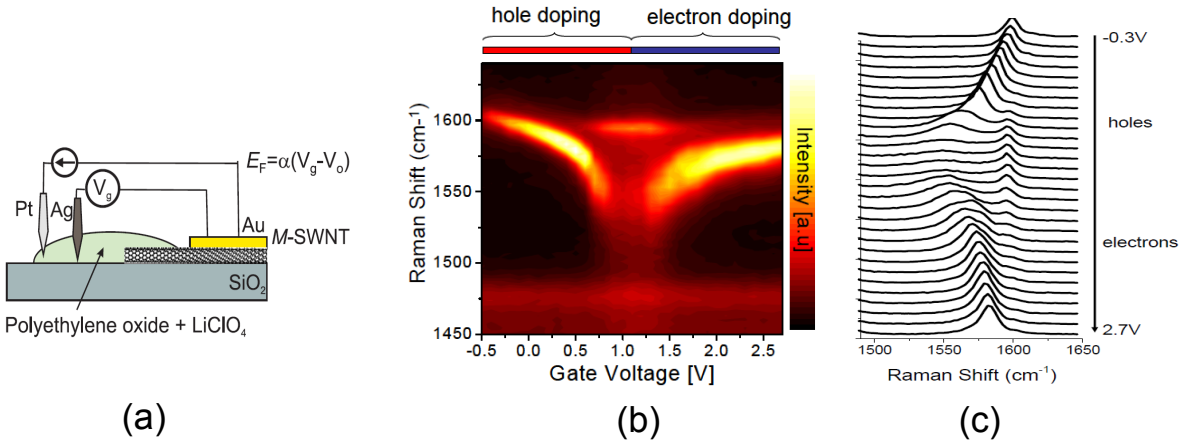

Figure 1-5: A schematic diagram of the electrochemical gating setup. A Pt counter electrode is used to maintain the gate voltage V_g between the Au contacted m-SWNT and a Ag pseudoreference electrode. The gate efficiency α, and charge neutrality voltage V_o relate V_g to E_F [6]. (b) G band intensity map as a function of gate voltage V_G. (c) G band spectrum taken at the indicated V_G values [15].

a electron-hole pair in the linear energy band of m-SWNTs. Figure 1-5(b) and (c) indicate that the presence of gate voltage, which give the E_F shift to positive and negative value, thus electron-hole pair excitation near linear energy band is no longer allowed. In both cases, the phonon energy is larger than that of neutral condition (no hole and no electron doping). In other words, in the absence of gate voltage, the phonon energy decreases due to electron hole excitation near E_F by means of electron-phonon interaction [16]. This phenomenon is indicated by gate-voltage dependence of a phonon spectral width and peak intensity position of the RBM, G and G′ bands [16, 17, 18]. In this thesis, this technique is utilized to prove that the ERS spectra comes from the single particle electron-hole pairs excitation.

1.2.5 Breit-Wigner-Fano lineshape observed in carbon systems

Fano states that interference between a discrete excitation spectrum and a continuum spectrum can lead to the asymmetric spectra, known as the Breit-Wigner-Fano (BWF) line-

Fig. 1-5: fig/intro-gate.eps

shape [3]. This BWF lineshape is expressed by

$$I(\omega) = I_0 \frac{\left[1 + (\omega - \omega_0)/q_{\mathrm{BWF}}\Gamma\right]^2}{1 + \left[(\omega - \omega_0)/\Gamma\right]^2}, \tag{1.1}$$

where ω_0 is the spectral peak position, Γ is the spectral width, and $1/q_{\mathrm{BWF}}$ is the asymmetric factor due to the mixing of discrete and continuous states. If $1/q_{\mathrm{BWF}} = 0$, Eq. (1.1) gives a Lorentzian lineshape. This BWF lineshape exhibit in many physical phenomena and the following are some examples of BWF line shapes found in carbon systems.

The BWF feature in SWNTs is observed only in the G band of m-SWNTs, while the G band of s-SWNTs shows Lorentzian lineshape (Fig. 1-2). Figure 1-6(a) shows how the Raman spectra of m-SWNTs bundles are nicely fitted to the BWF formula (Eq. (1.1)). The origin of this asymmetric lineshape is widely believed to be a contribution of an electron excitation within the linear band of m-SWNTs.

In graphene, the G band Raman spectra also exhibit BWF lineshape (Fig. 1-6(b)). The spectral lineshape strongly depends on the Fermi energy which signifies the signature of electron contribution near the Fermi level.

In graphite intercalated compound (GIC), for example C_8Cs, donor atoms Cs are inserted between graphite layers. The contribution of donated electron gives the continuum spectra which modify the discrete phonon spectral shapes to be the BWF (Fig. 1-6(c)).

1.2.6 Exciton photo-physics in SWNTs

The exciton is an excitation of an electron-hole pair bounded by the Coulomb interaction. The signature of an exciton can be detected by observing a discrete bound state below the continuum single particle energy spectra, like in energy levels of a hydrogen atom below the continuum level [21]. In SWNTs, exciton binding energy is even observable at room temperature due to 1D quantum confinement [22, 23]. Two-photon photo luminescence experiment is one of the experimental evidence that the bound exciton states present in s-SWNTs at room temperature [24].

Figure 1-7(c) shows the luminescence map of excitation wavelength and emission wave-

Fig. 1-6: fig/ch1-bwf-gic.eps

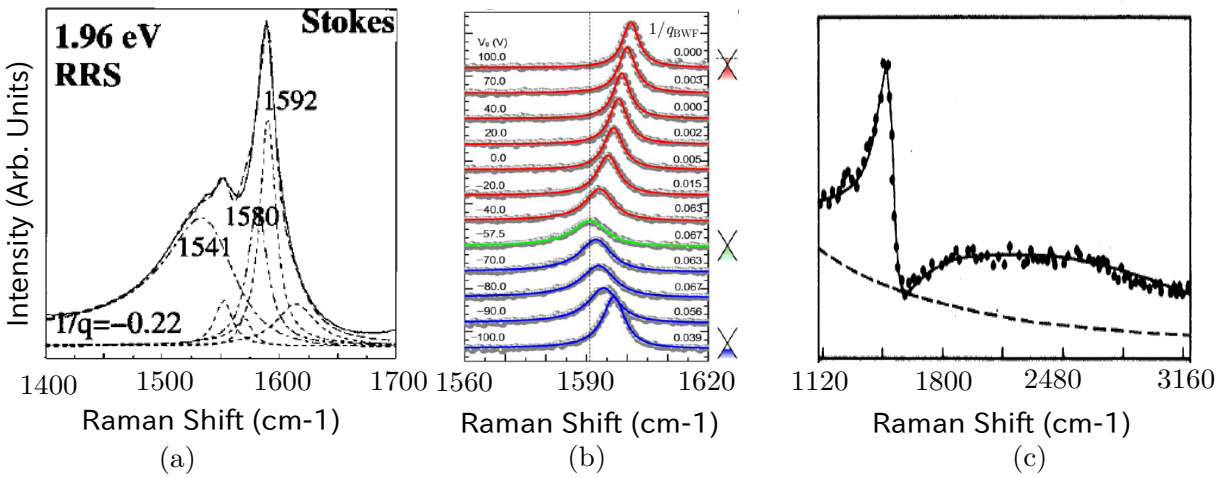

Figure 1-6: Examples of BWF lineshapes found in carbon materials. (a) m-SWNTs bundle [2], (b) graphene with asymmetric factor ($1/q_{BWF}$) changes as a function of Fermi energy [19], and (c) graphite intercalated compound (C_8Cs) [20]

length. By applying laser excitation energy below the band gap 1210 nm (1.02 eV) and 1970 nm (0.6 eV), for each nanotube it found that the emission energy is far larger than the excitation energy, from 1.18 eV (1050 nm) to 1.37 eV (900 nm). This figure is assigned as two-photon absorption process (Fig. 1-7(b)). However, this emission energy is lower than twice of the excitation energy. Maultzsch et al. argue that the energy shift is due to the relaxation of exciton from $2g$ state to $1u$ state and thus signifies the existence of the exciton state at room temperature. u (g) is the odd (even) excitonic states symmetry with respect to C_2 rotation about the axis passing through the center of hexagon and perpendicular to the tube axis (U-axis). $n = 1, 2$ indicate the n exciton eigen states. Emission occurs from the lowest one-photon active $1u$ states. From this measurement, we found that exciton binding energy for s-SWNTs is around 300-400 meV, which is a quarter of SWNTs' energy gap.

The existence of excitons is not only observable in s-SWNTs but also in m-SWNTs. Wang et al. found that absorption spectra in m-SWNTs, in spite of the screening effect which weaken the Coulomb interaction, exciton binding energy is observed to be ~ 50 meV [25, 26].

Exciton effect is essential to understand the optical process in SWNTs. Exciton binding energy modifies the optical transition energy (E_{ii}) from that of single particle picture. The

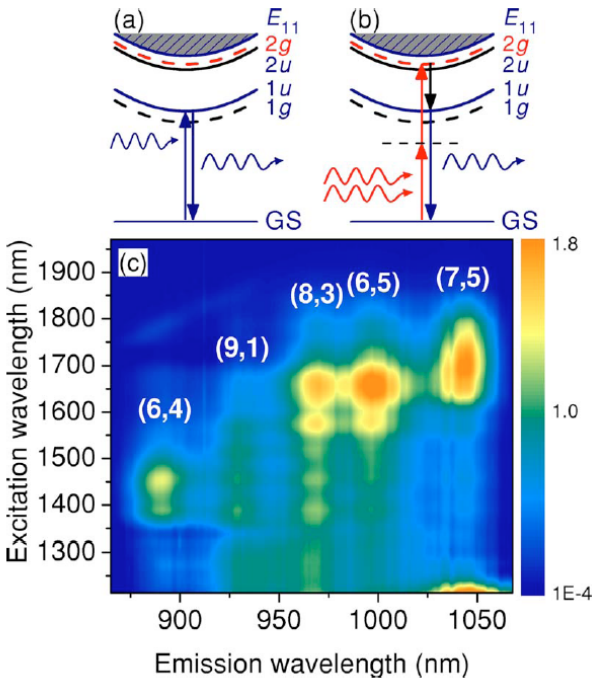

Figure 1-7: (a) Schematic diagram of one-photon absorption and emission in SWNTs. E_{11} indicates the single particle transition between the lowest subbands. u (g) is the odd (even) excitonic states symmetry with respect to C_2 rotation about the axis passing through the center of hexagon and perpendicular to the tube axis (U-axis). $n = 1, 2$ indicate the n exciton eigen states. Emission occurs from the lowest one-photon active $1u$ states. (b) Two-photon absorption result. (c) Two-photon luminescence spectra [24].

environment effect of (E_{ii}) can be discussed from dielectric screening effect which modifies exciton binding energy [27, 28, 29, 30].

Fig. 1-7: fig/ch1-exciton.eps

Chapter 2

Electronic and Excitonic Properties of Single Wall Carbon Nanotubes

In this chapter, the electronic properties of single wall carbon nanotubes (SWNTs) are reviewed. The SWNTs geometry is obtained from rolling up the single-layer graphite (graphene), therefore the electronic structure of SWNTs can be derived from the electronic structure of graphene. The electronic structure of graphene and SWNTs are calculated with tight binding methods. In Sec. 2.1.1-2.1.5, we will use simple tight binding method (STB) to understand the basic electronic structure of graphene and SWNTs. In Sec. 2.1.6, we will discuss the limitation of STB method and will introduce the extended tight binding (ETB) method in order to improve calculations. All detailed derivations and important definitions will be explained below.

2.1 Electronic Properties of Graphene and SWNTs

2.1.1 Graphene unit cell and Brillouin zone

Graphene is a single atomic layer of two dimensional (2D) hexagonal carbon lattice whose structure is considered the basic building block of sp^2 carbon allotropes. The carbon-carbon atoms of graphene are bound by covalent bondings (σ-bonds) to form the graphene layer. Several layers of graphene sheets are stacked together by the van der Waals force to form

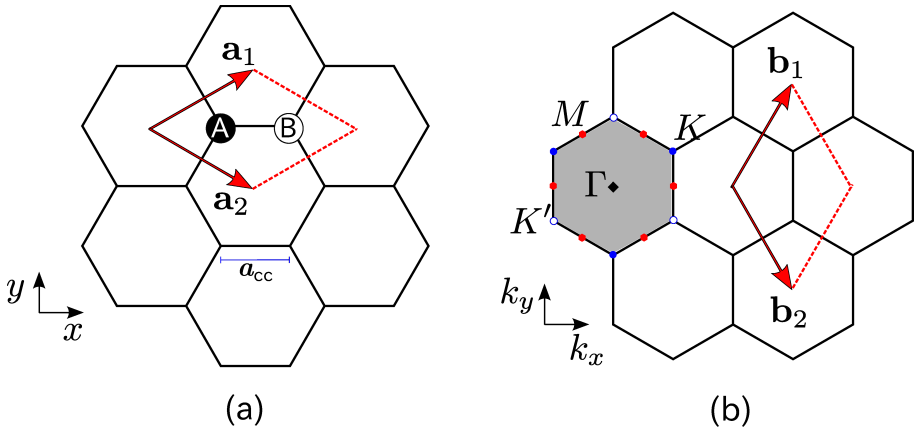

Figure 2-1: (a) The unit cell of graphene which consists of two atomic sites A and B. $\mathbf{a}_1$, and $\mathbf{a}_2$ are the unit vectors and a_{cc} is the carbon-carbon distance. (b) Brillouin zone of graphene. Γ, K, K$'$, and M indicated with a closed diamond, closed circles, opened circles, and closed hexagons, respectively, are the high symmetry points. Reciprocal lattice vectors is denoted by $\mathbf{b}_1$ and $\mathbf{b}_2$.

three dimensional (3D) graphite. A graphene sheet can be wrapped up to form a 0D fullerene and can be rolled up to form a 1D SWNT.

Figure 2-1 gives the unit cell and Brillouin zone of graphene. Unit vectors $\mathbf{a}_1$ and $\mathbf{a}_2$ are given by

$$\mathbf{a}_1 = a\left(\frac{\sqrt{3}}{2}, \frac{1}{2}\right), \quad \mathbf{a}_2 = a\left(\frac{\sqrt{3}}{2}, -\frac{1}{2}\right), \tag{2.1}$$

where $a = \sqrt{3}a_{cc}$ is the lattice constant for the graphene unit cell and $a_{cc} = 0.142$nm is the nearest carbon-carbon distance. Reciprocal lattice vectors $\mathbf{b}_1$ and $\mathbf{b}_2$ are obtained from the relations:

$$\mathbf{a}_i\mathbf{b}_j = 2\pi\delta_{ij}, \tag{2.2}$$

where δ_{ij} is the Kronecker's delta ($\delta_{ij} = 1$ for $i = j$, $\delta_{ij} = 0$ otherwise) and $\mathbf{b}_1$ and $\mathbf{b}_2$ are given by

$$\mathbf{b}_1 = \frac{2\pi}{a}\left(\frac{1}{\sqrt{3}}, 1\right), \quad \mathbf{b}_2 = \frac{2\pi}{a}\left(\frac{1}{\sqrt{3}}, -1\right). \tag{2.3}$$

The first Brillouin zone is the rhombic area enclosed by $\mathbf{b}_1$ and $\mathbf{b}_2$ as shown in Fig. 2-1(b). That Brillouin zone area is equivalent to the shaded hexagon. The high symmetry points are defined at center Γ, the center of an edge M, and the hexagonal corners K and K$'$ of

Fig. 2-1: fig/grapbz.eps

the Brillouin zone which are very useful to simplify the analysis of electronic structure in Graphene (Sec. 2.1.2).

2.1.2 Electronic structure of graphene

The electronic dispersion relations of graphene is reviewed within the tight-binding method, starting from a simple tight-binding (STB) method. A STB method (or linear combination of atomic orbitals, LCAO) is used to calculate the electronic energy dispersion relation of a crystal, that is the energy E as a function of wavevector $\mathbf{k}$. In the tight binding approximation of a crystal, the eigenfunctions of electrons are made up by Bloch function corresponding to atomic orbitals.

Thus the problem of finding an eigenfunction is reduced to finding the coefficients for the Bloch function consisting of atomic orbitals. Per one unit cell of graphene, we have 5 atomic orbitals (1s, 2s, $2p_x$, $2p_y$, and $2p_z$) from each A and B atomic site (Fig. 2-1(a)), which give 10 atomic orbitals all together in the unit cell. The valence electrons (2s, $2p_x$, and $2p_y$) construct a sp^2 hybridization (σ bond) and $2p_z$ orbital gives the π bonding. Hereafter, in STB method we consider only π electron since its energy is very close to Fermi energy and it dominantly contributes to electronic transport and optical properties. In the case of small diameter SWNTs, because of curvature effect, we should take into account the mixing of $\sigma - \pi$ electrons [31, 32].

The electron wavefunction for band with index j is given by given by

$$\psi^j(\mathbf{k}, \mathbf{r}) = \sum_{s=\mathrm{A,B}} C_s^j(\mathbf{k}) \phi_s(\mathbf{k}, \mathbf{r}), \quad (j = 1, 2). \tag{2.4}$$

Here $j = 1, 2$ is the electronic energy band index for π bonding (valence band) and π^* anti-bonding (conduction band), respectively and s in the sum is taken over A and B atomic sites. The $C_s^j(\mathbf{k})$ are wavefunction coefficients for the Bloch functions $\phi_s(\mathbf{k}, \mathbf{r})$. The Bloch wavefunctions are given by a sum over the atomic wavefunctions φ_s for each orbital at the u–th crystal site multiplied by a phase factor $e^{i\mathbf{k}\cdot\mathbf{R}_s^u}$. The atomic orbital φ_s in the u unit cell

is centered at $\mathbf{R}_s^u$.

$$\phi_s(\mathbf{k},\mathbf{r}) = \frac{1}{\sqrt{U}} \sum_{u=0}^{U-1} e^{i\mathbf{k}\cdot\mathbf{R}_s^u} \varphi_s(\mathbf{r}-\mathbf{R}_s^u), \quad (s=\mathrm{A},\mathrm{B})\,. \tag{2.5}$$

We solve the energy for eigen state j by minimizing

$$E^j = \frac{\langle\psi^j|H|\psi^j\rangle}{\langle\psi^j|\psi^j\rangle}, \quad (j=1,2), \tag{2.6}$$

as a function of the wavefunction coefficients. The variational condition for finding the minimum is

$$\frac{\partial E^j}{\partial C_s^{j*}} = 0, \quad (j=1,2). \tag{2.7}$$

The resulting equations for $C_s^j(\mathbf{k})$ after minimization Eq. (2.7) are

$$\sum_{s'} H_{\mathrm{ss}'} C_{s'}^j(\mathbf{k}) = E^j \sum_{s'} S_{\mathrm{ss}'} C_{s'}^j(\mathbf{k}) \quad (s,s'=\mathrm{A},\mathrm{B}), \tag{2.8}$$

where $H_{ss'} = \langle\phi_s|H|\phi_{s'}\rangle$ is the transfer matrix and $S_{ss'} = \langle\phi_s|\phi_{s'}\rangle$ is the overlap matrix. We may write explicitly the matrix elements in Eq. (2.8) as

$$H(\mathbf{k}) = \begin{pmatrix} H_{\mathrm{AA}}(\mathbf{k}) & H_{\mathrm{AB}}(\mathbf{k}) \\ H_{\mathrm{BA}}(\mathbf{k}) & H_{\mathrm{BB}}(\mathbf{k}) \end{pmatrix}, \quad \text{and} \quad S(\mathbf{k}) = \begin{pmatrix} S_{\mathrm{AA}}(\mathbf{k}) & S_{\mathrm{AB}}(\mathbf{k}) \\ S_{\mathrm{BA}}(\mathbf{k}) & S_{\mathrm{BB}}(\mathbf{k}) \end{pmatrix}. \tag{2.9}$$

Because $H(\mathbf{k})$ and $S(\mathbf{k})$ should form Hermitian matrices, we require

$$H_{\mathrm{BA}}(\mathbf{k}) = H_{\mathrm{AB}}^*(\mathbf{k}), \quad \text{and} \quad S_{\mathrm{BA}}(\mathbf{k}) = S_{\mathrm{AB}}^*(\mathbf{k}). \tag{2.10}$$

Now we evaluate each component of matrix elements. By using Eq. (2.5),

$$\begin{aligned} H_{\mathrm{AA}}(\mathbf{k}) &= \frac{1}{U} \sum_{\mathbf{R},\mathbf{R}'} e^{i\mathbf{k}.(\mathbf{R}-\mathbf{R}')} \langle\varphi_A(\mathbf{r}-\mathbf{R}')|H|\varphi_A(\mathbf{r}-\mathbf{R})\rangle \\ &= \epsilon_{2\mathrm{p}} + \mathcal{O}(\mathbf{R} \geq \mathbf{R} \pm \mathbf{a}_i). \end{aligned} \tag{2.11}$$

By neglecting the higher order distance $\mathbf{R} \geq \mathbf{R} \pm \mathbf{a}_i$ contribution, for simplicity, H_{AA} gives

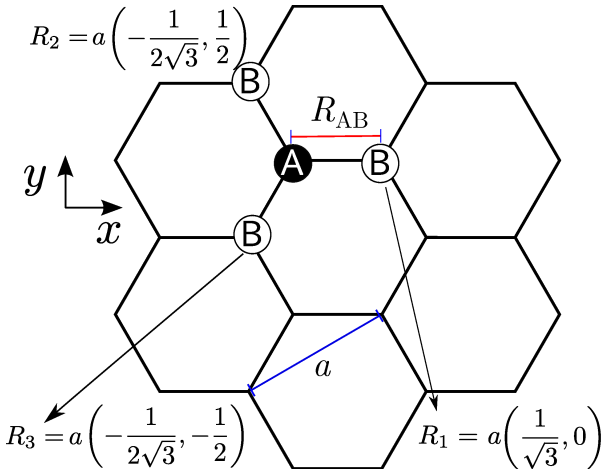

Figure 2-2: A and B atomic site of a graphene unit cell. A atom lies at center $(0, 0)$ and three nearest neighbor B atoms are indicated by R_1, R_2, and R_3 with their (x, y) coordinates are given. $a = 2.46$ Å

the orbital energy of $2p$ level, $\epsilon_{2\mathrm{p}}$. In the same manner, H_{BB} gives the same $\epsilon_{2\mathrm{p}}$. Since the difference of H_{AA} and H_{BB} is more important than their value itself, we may set $H_{\mathrm{AA}} = H_{\mathrm{BB}} = 0$ which just change the energy threshold.

For $H_{\mathrm{AB}}(\mathbf{k})$ using the same method as above, the largest contribution of matrix elements arise when atoms A and B are nearest neighbors with distance $\mathbf{R}_i$, $(i = 1, \ldots, 3)$ for the first nearest neighbors (Fig. 2-2). Thus we only consider $\mathbf{R}' = \mathbf{R} + \mathbf{R}_i$ in the summation over $\mathbf{R}'$ and neglecting the more distant term to obtain

$$\begin{aligned} H_{\mathrm{AB}}(\mathbf{k}) &= \frac{1}{U}\sum_{\mathbf{R},i} e^{i\mathbf{k}.\mathbf{R}_i}\langle\varphi_{\mathrm{A}}(\mathbf{r}-\mathbf{R})|H|\varphi_{\mathrm{B}}(\mathbf{r}-\mathbf{R}-\mathbf{R}_i), \quad i = 1, \ldots 3 \\ &\equiv tf(\mathbf{k}) \end{aligned} \tag{2.12}$$

where $t = -3.033$ eV [33] is the transfer matrix $\langle\varphi_{\mathrm{A}}(\mathbf{r}-\mathbf{R})|H|\varphi_{\mathrm{B}}(\mathbf{r}-\mathbf{R}-\mathbf{R}_{\mathrm{AB}})\rangle$ which are the same for three nearest neighbor B atoms in Fig. 2-2, and $f(\mathbf{k})$ is a function of the sum of the phase factor $f(\mathbf{k}) = \sum_{i=1}^{3} e^{i\mathbf{k}.\mathbf{R}_i}$. By using x, y coordinates of Fig. 2-2, $f(\mathbf{k})$ is given by

$$f(\mathbf{k}) = e^{ik_x a/\sqrt{3}} + 2e^{-ik_x a/2\sqrt{3}} \cos\left(\frac{k_y a}{2}\right). \tag{2.13}$$

Fig. 2-2: fig/ch2-ab.eps

Using Eq. (2.5), the overlap integral $S_{\rm AA} = S_{\rm BB} = 1$, and $S_{\rm AB} = sf(\mathbf{k}) = S^*_{\rm BA}$. Here the overlap parameter s is defined by

$$s = \langle \varphi_{\rm A}(\mathbf{r} - \mathbf{R}) | \varphi_{\rm B}(\mathbf{r} - \mathbf{R} - \mathbf{R}_{\rm AB}) \rangle. \tag{2.14}$$

In this work, we take $s = 0.129$ [33] in order to reproduce the result from first principle calculation of graphite energy bands. Combining Eqs. (2.9)-(2.14), Eq.(2.8) becomes,

$$\begin{pmatrix} -E^i(\mathbf{k}) & f(\mathbf{k})\{t - sE^i(\mathbf{k})\} \\ f^*(\mathbf{k})\{t - sE^i(\mathbf{k})\} & -E^i(\mathbf{k}) \end{pmatrix} \begin{pmatrix} C^i_A(\mathbf{k}) \\ C^i_B(\mathbf{k}) \end{pmatrix} = \mathbf{0}\ , \quad (i = \mathrm{c},\ \mathrm{v}). \tag{2.15}$$

The solution of Eq. (2.15) is given by

$$E^{\pm}_g(\mathbf{k}) = \frac{\pm t w(\mathbf{k})}{1 \pm s w(\mathbf{k})} \tag{2.16}$$

where $w(\mathbf{k}) = \sqrt{f(\mathbf{k}) f^*(\mathbf{k})}$ Now we use $E_g(\mathbf{k})$ notation for graphene energy dispersion relation and to distinguish it from $E(\mathbf{k})$, SWNT energy dispersion. $+$ $(-)$ sign denotes the valence (conduction) band, by noting that t has a negative value. The electronic structure of π electron now can be obtained by mapping $E_g(\mathbf{k})$ over first Brillouin zone in Fig. 2-1(b). In Fig. 2-3(a), the 3D picture of $E(\mathbf{k})$ in the first Brillouin zone is plotted. $E^{\pm}_g$ bands touch each other at K and K$'$ points.

For a small electron wavevector $\mathbf{k}$, which is measured from K points, we expand Eq. (2.16) around K and K$'$ as $f(\mathbf{K} + \mathbf{k})$ and $f(\mathbf{K}' + \mathbf{k})$. The K and K$'$ points have coordinates $\mathbf{K} = (0, -4\pi/(3a))$ and $\mathbf{K}' = (0, 4\pi/(3a))$. With $\mathbf{k} = (k_x, k_y)$ we obtain

$$f(\mathbf{K} + \mathbf{k}) = \frac{\sqrt{3}a}{2}(ik_x + k_y), \quad \text{and} \quad f(\mathbf{K}' + \mathbf{k}) = \frac{\sqrt{3}a}{2}(ik_x - k_y)\,. \tag{2.17}$$

Substituting Eqs. (2.17) into Eq. (2.16), we get an approximation for the electron energy dispersion relations close to K points. It turns out that in the linear order approximation we get the same energy dispersion relation around K and K$'$ points,

$$E^{\pm}_g(\mathbf{k} + \mathbf{K}) = \pm \frac{\sqrt{3}at}{2}\sqrt{k_x^2 + k_y^2}. \tag{2.18}$$

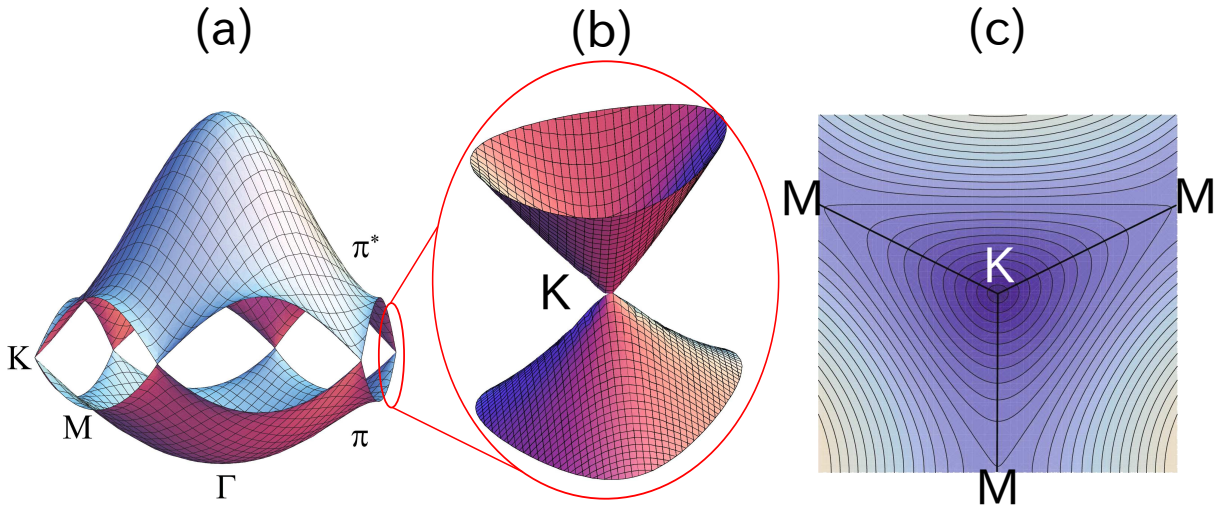

Figure 2-3: (a) π electron energy dispersion relation in the first Brillouin zone from Eq. (2.16). (b) Dirac-cone around K point (Eq. (2.17)). (c) Equi–energy contour of $E_g(\mathbf{k})$ which shows circle near K point and deform to triangle, known as trigonal warping effect [34], if we go further to M point. Separation between two equi-energy lines are 0.7 eV.

Here the "+(–)" sign corresponds to valence (conduction) band. In Fig. 2-3(b), we plot the $E(\mathbf{k})$ for Eq. (2.18) which has a cone shape, known as the Dirac cone. In Fig. 2-3(c) we plot equi–energy contours which are almost circles around K and K points. The equi–energy circles deform to triangles, when going to higher electron energies. This is known as the trigonal warping effect in graphene [34]. The equi–energy contour connecting three nearest M points is a triangle as shown in Fig. 2-3(c). Optical transitions occur between bonding and anti–bonding bands and from Fig. 2-3(a) it is clear that low energy optical spectroscopy in the region of visible light mainly probes electrons around K points between the π and π^* bands.

We now calculate the wavefunction coefficients for electrons for A and B atoms, $C^i_{\rm A}$ and $C^i_{\rm B}$, respectively. The wavefunction coefficients are the eigenvectors that are obtained by solving Eq. (2.15). The normalization and orthonormality condition is $\langle\psi^i(\mathbf{r},\mathbf{k})|\psi^j(\mathbf{r},\mathbf{k})\rangle = \delta_{ij}$ where $\psi^i(\mathbf{r},\mathbf{k}) = C^i_{\rm A}(\mathbf{k})\phi_{\rm A}\mathbf{r},\mathbf{k}) + C^i_{\rm B}(\mathbf{k})\phi_{\rm B}(\mathbf{r},\mathbf{k})$. Here, $C^i_{\rm A}(\mathbf{k})$ and $C^i_{\rm B}(\mathbf{k})$ are the wavefunction coefficients, which are the eigenvectors of Eq. (2.15). By putting the possible indices for i and j, we can obtain four equations, that are needed to calculate the four wavefunction coefficients ($C^j_{\rm A}$, $C^j_{\rm B}$ for $j = {\rm c}, {\rm v}$) of the Bloch functions. The orthonormality conditions can

Fig. 2-3: fig/ch2-triek.eps

be expanded in terms of Bloch functions as

$$\begin{aligned}\langle\psi^i(\mathbf{r},\mathbf{k})|\psi^j(\mathbf{r},\mathbf{k})\rangle =& C_A^{*i}C_A^j\langle\phi_A(\mathbf{r})|\phi_A(\mathbf{r})\rangle + C_A^{*i}C_B^j\langle\phi_A(\mathbf{r})|\phi_B(\mathbf{r})\rangle \\ &+ C_B^{*i}C_A^j\langle\phi_B(\mathbf{r})|\phi_A(\mathbf{r})\rangle + C_B^{*i}C_B^j\langle\phi_B(\mathbf{r})|\phi_B(\mathbf{r})\rangle. \end{aligned} \tag{2.19}$$

Using the Bloch functions in Eq. (2.5) which are also normalized, we get $\langle\phi_A(\mathbf{r})|\phi_A(\mathbf{r})\rangle = 1$ and $\langle\phi_B(\mathbf{r})|\phi_B(\mathbf{r})\rangle = 1$. Thus the orthonormality conditions give

$$\begin{aligned}\langle\psi^i(\mathbf{r},\mathbf{k})|\psi^j(\mathbf{r},\mathbf{k})\rangle =& C_A^{*i}(\mathbf{k})C_A^j(\mathbf{k}) + sf(\mathbf{k})C_A^{*i}(\mathbf{k})C_B^j(\mathbf{k}) \\ &+ C_B^{*i}(\mathbf{k})C_B^j(\mathbf{k}) + sf^*(\mathbf{k})C_B^{*i}(\mathbf{k})C_A^j(\mathbf{k}) = \delta_{ij} \\ &(i = \mathrm{v},\ \mathrm{c} \text{ and } j = \mathrm{v},\ \mathrm{c}). \end{aligned} \tag{2.20}$$

The relation between C_{A}^j and C_{B}^j is obtained from Eq. (2.15) and is given by

$$C_{\mathrm{A}}^i(\mathbf{k}) = C_{\mathrm{B}}^i(\mathbf{k})\frac{f(\mathbf{k})}{E^i(\mathbf{k})}\left\{t - sE^i(\mathbf{k})\right\}. \tag{2.21}$$

To calculate coefficient $C_{\mathrm{A}}^i(\mathbf{k})$ for $i = \mathrm{v},\ \mathrm{c}$, we consider $\langle\psi^i(\mathbf{r},\mathbf{k})|\psi^i(\mathbf{r},\mathbf{k})\rangle = 1$. We expand $\Psi^i(\mathbf{r},\mathbf{k})$ into Bloch functions and use Eq. (2.21) to replace $C_{\mathrm{B}}^i(\mathbf{k})$ by $C_{\mathrm{A}}^i(\mathbf{k})$. Noting that

$$\frac{E_{\mathrm{c}}(\mathbf{k})}{t - sE_{\mathrm{c}}(\mathbf{k})} = -w(\mathbf{k}) \quad \text{and} \quad \frac{E_{\mathrm{v}}(\mathbf{k})}{t - sE_{\mathrm{v}}(\mathbf{k})} = w(\mathbf{k}), \tag{2.22}$$

we can obtain the coefficients for B atoms as

$$C_{\mathrm{B}}^{\mathrm{v}}(\mathbf{k}) = C_{\mathrm{A}}^{\mathrm{v}}\frac{f^*(\mathbf{k})}{w(\mathbf{k})} \quad \text{and} \quad C_{\mathrm{B}}^{\mathrm{c}}(\mathbf{k}) = -C_{\mathrm{A}}^{\mathrm{c}}\frac{f^*(\mathbf{k})}{w(\mathbf{k})}. \tag{2.23}$$

We can then obtain $C_{\mathrm{A}}^i(\mathbf{k})$ for $i = \mathrm{v},\ \mathrm{c}$ as

$$\begin{aligned} C_{\mathrm{A}}^{\mathrm{v}}(\mathbf{k}) &= \exp(i\phi_{\mathrm{v}})\sqrt{\frac{1}{2\left\{1 + sw(\mathbf{k})\right\}}} \quad \text{and} \quad C_{\mathrm{A}}^{\mathrm{c}}(\mathbf{k}) = \exp(i\phi_{\mathrm{c}})\sqrt{\frac{1}{2\left\{1 - sw(\mathbf{k})\right\}}}, \\ C_{\mathrm{B}}^{\mathrm{v}}(\mathbf{k}) &= \exp\left[i(\phi_{\mathrm{v}} + \theta(f^*)\right]\sqrt{\frac{1}{2\left\{1 + sw(\mathbf{k})\right\}}} \quad \text{and} \quad C_{\mathrm{B}}^{\mathrm{c}}(\mathbf{k}) = -\exp\left[i(\phi_{\mathrm{c}} + \theta(f^*)\right]\sqrt{\frac{1}{2\left\{1 - sw(\mathbf{k})\right\}}}. \end{aligned} \tag{2.24}$$

where $\tan\theta(f^*) = \mathrm{Im}(f^*)/\mathrm{Re}(f^*)$. Note that the phasefactors ϕ_v or ϕ_c for Eq. (2.24) can be chosen arbitrarily as long as the phase difference between A and B atoms preserve. The symmetry of wave function coefficients ($C^j_\mathrm{A},\ C^j_\mathrm{B}$ for $j = \mathrm{c}, \mathrm{v}$) play an important role of vanishing the direct Coulomb interaction at zero momentum transfer which will be discussed in Section 3.3

2.1.3 SWNT unit cell and Brillouin zone

After discussing the electronic structure of graphene, now we review the electronic structure of SWNTs with the same simple tight binding method. SWNTs unit cell and Brillouin zone are defined in the 2D hexagonal plane as shown below. Then we adapt the simple tight binding method for calculating electronic structure and density of states of a SWNT.

In Fig. 2-4, we show the unrolled unit cell of a SWNT expressed by rectangle ORQP. The unit cell forms the rectangle ORQP specified by the chiral vector $\mathbf{C_h}$ and the translational vector $\mathbf{T}$. SWNT can be constructed by connecting O to R and P to Q. $\overrightarrow{OR}$ and $\overrightarrow{OP}$ define the chiral vector $\mathbf{C_h}$ (the way to roll up the unit cell) and translational vector $\mathbf{T}$ (direction of tube axis), respectively.

$\mathbf{C_h}$ is defined in terms of the unit vector of graphene $\mathbf{a}_1$ and $\mathbf{a}_2$,

$$\mathbf{C_h} = n\mathbf{a}_1 + m\mathbf{a}_2 \equiv (n, m), \tag{2.25}$$

where $n,\ m$ are positive or zero integers with $n \geq m > 0$. The circumferential length L of a SWNT is nothing but the length of $\mathbf{C_h}$:

$$L = |\mathbf{C_h}| = a\sqrt{n^2 + nm + m^2}, \tag{2.26}$$

the tube diameter d_t can be determined by L/π,

$$d_t = \frac{L}{\pi} = \frac{a\sqrt{n^2 + nm + m^2}}{\pi}. \tag{2.27}$$

Fig. 2-4: fig/ch2-swnt-uc.eps

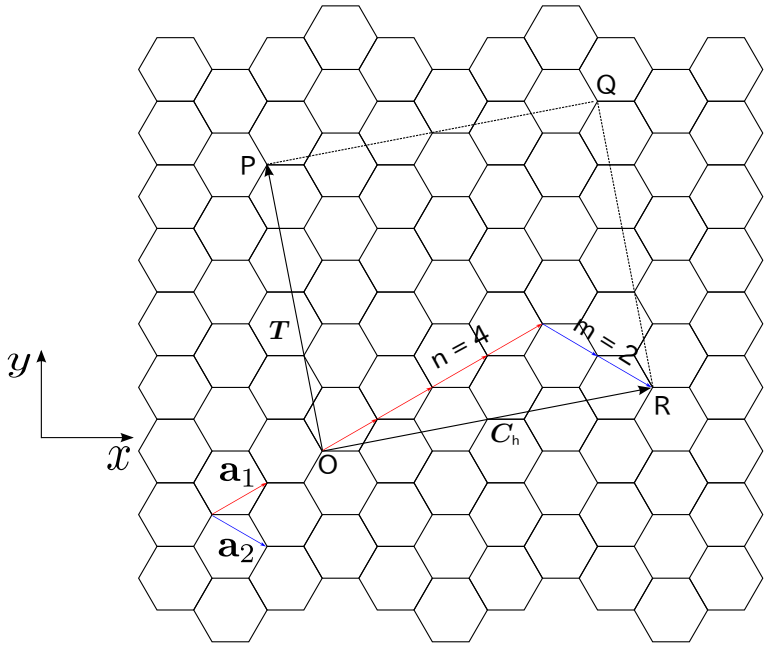

Figure 2-4: Rectangle $OPQR$ is the unrolled unitcell of a (4,2) SWNT. SWNT can be constructed by connecting O to R and P to Q. $\overrightarrow{OR}$ and $\overrightarrow{OP}$ define the chiral vector $\mathbf{C_h}$ and translational vector $\mathbf{T}$, respectively. In this figure, $\mathbf{C_h} = (4, 2)$, $\mathbf{T} = (4, -5)$, and number of hexagons in the SWNT unit cell $N = 28$.

The vector $\mathbf{T}$ is determined by

$$\mathbf{T} = t_1\mathbf{a}_1 + t_2\mathbf{a}_2 \equiv (t_1, t_2), \tag{2.28}$$

where t_1 and t_2 are integers determined by the relations $\mathbf{C_h} \cdot \mathbf{T} = 0$. Using Eqs. (2.25) and (2.28), we get

$$t_1 = \frac{2m + n}{d_R}, \quad t_2 = -\frac{2n + m}{d_R} \tag{2.29}$$

where d_R is the greatest common divisor (gcd) of $(2m+n)$ and $(2n+m)$ so that $\gcd(t_1, t_2) = 1$.

The absolute value of vector product $|\mathbf{C_h} \times \mathbf{T}|$ determines the area of a SWNT unit cell $OPQR$ (Fig. 2-4), while $|\mathbf{a}_1 \times \mathbf{a}_2|$ equals the area of a graphene hexagon. Relating those two values, number of hexagons N within a SWNT unit cell, is given by:

$$N = \frac{|\mathbf{C_h} \times \mathbf{T}|}{|\mathbf{a}_1 \times \mathbf{a}_2|} = \frac{2(n^2 + m^2 + nm)}{d_R}. \tag{2.30}$$

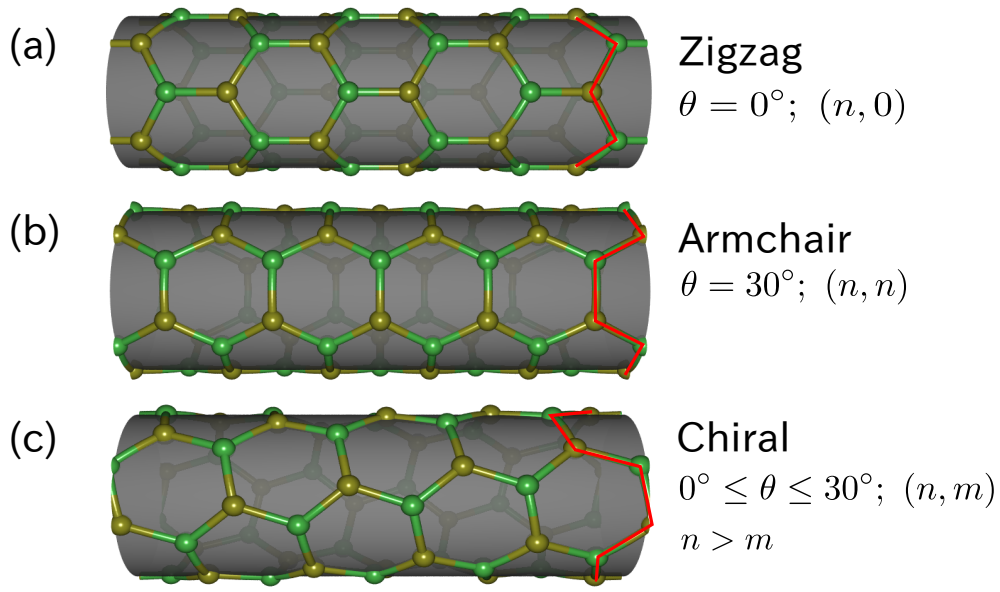

Figure 2-5: Classification of SWNTs: (a) zigzag, (b) armchair, (c) chiral SWNTs. From left to right, the chiral index of each SWNT above is $(5, 0)$, $(3, 3)$, $(4, 2)$, respectively. The shape of cross section is given by a red line.

The chiral angle θ is defined by an angle between $\mathbf{C_h}$ and $\mathbf{a}_1$

$$\cos\theta = \frac{\mathbf{C_h} \cdot \mathbf{a}_1}{|\mathbf{C_h}||\mathbf{a}_1|} = \frac{2n + m}{2\sqrt{n^2 + m^2 + nm}}. \tag{2.31}$$

θ determines the spiral geometry of SWNTs which can be seen in the edge structure (red lines in Fig. 2-5). $\theta = 0^o$ and $\theta = 30^o$ correspond to zigzag $(n, 0)$ and armchair (n, n) SWNTs, respectively, and chiral SWNTs, (n, m) with $n > m > 0$ have $0 < \theta < 30^o$. Those three types of SWNTs are depicted in Fig. 2-5.

The reciprocal lattice vectors $\mathbf{K_1}$ and $\mathbf{K_2}$ of a SWNT is determined by the relation:

$$\begin{aligned} \mathbf{C_h} \cdot \mathbf{K_1} &= 2\pi, & \mathbf{T} \cdot \mathbf{K_1} &= 0, \\ \mathbf{C_h} \cdot \mathbf{K_2} &= 0, & \mathbf{T} \cdot \mathbf{K_2} &= 2\pi. \end{aligned} \tag{2.32}$$

Using Eqs (2.25), (2.28), and (2.32), we get expressions for $\mathbf{K_1}$ and $\mathbf{K_2}$:

$$\mathbf{K_1} = \frac{1}{N}(-t_2\mathbf{b}_1 + t_1\mathbf{b}_2), \quad \mathbf{K_2} = \frac{1}{N}(m\mathbf{b}_1 - n\mathbf{b}_2), \tag{2.33}$$

Fig. 2-5: fig/ch2-swntclass.eps

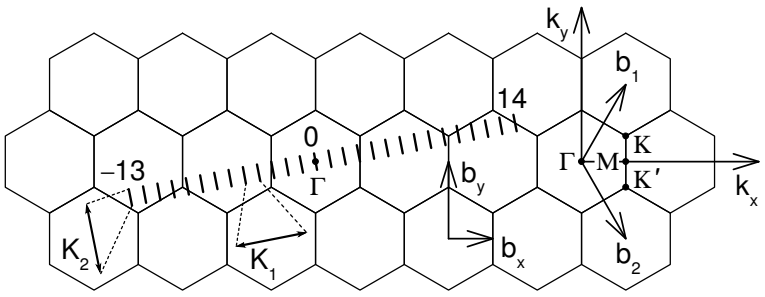

Figure 2-6: The reciprocal lattice vectors $\mathbf{K_1}$ and $\mathbf{K_2}$, and the Brillouin zone of a $(4, 2)$ swnt represented by the set of $N = 28$ parallel cutting lines. The cutting lines are labeled by the integer angular momentum index μ $\left\{\mu = -\left(\frac{N}{2} - 1\right), ..., \frac{N}{2}\right\}$ with $\mu = 0$ correspond to a cutting line which passes through Γ point.

In Fig. 2-6, we show the reciprocal lattice vectors, $\mathbf{K_1}$ and $\mathbf{K_2}$, for $\mathbf{C_h} = (4, 2)$ SWNT. One segment of line with length $|\mathbf{K_2}| = 2\pi/|\mathbf{T}|$ is the first Brillouin zone of a 1D SWNT. From the expression of $\mathbf{K_1}$ in Eq. (2.33), we know that two wave vectors differ by $N\mathbf{K_1}$ are equivalent, in this case $N = 28$. Thus we have quantized N wave vectors $\mu\mathbf{K_1}$ $\left\{\mu = -\left(\frac{N}{2} - 1\right), ..., \frac{N}{2}\right\}$ which arise from boundary condition along circumferential direction $\mathbf{C_h}$. We have quasi-continuous wave vectors in $\mathbf{K_2}$ direction because of the periodicity along the tube axis $\mathbf{T}$ in 1D SWNTs. But if we have a finite length L_t SWNT, we will have a discrete k point in $\mathbf{K_2}$ direction separated with a distance $2\pi/L_t$. Combination of discrete and quasi-continuous lines resemble 1D SWNTs Brillouin zone,

$$\mathbf{k} = k\frac{\mathbf{K_2}}{|\mathbf{K_2}|} + \mu\mathbf{K_1}, \quad \left\{\mu = -\left(\frac{N}{2} - 1\right), ..., \frac{N}{2}, \text{ and } -\frac{\pi}{T} < k < \frac{\pi}{T}\right\}, \tag{2.34}$$

which is called cutting lines [35]. Note that $|\mathbf{K_1}| = \frac{2}{d_t}$ and $|\mathbf{K_2}| = \frac{2\pi}{T}$ which will be used later.

2.1.4 Electronic structure of SWNTs

The electronic structure of SWNTs can be obtained directly from that of graphene. As shown in Sec. 2.1.3, SWNTs wave vector composes of quasi-continuous k points in the tube axis direction $\mathbf{K_2}$, and quantized μ wave vector along the circumferential direction $\mathbf{K_1}$ (Eq.

Fig. 2-6: fig/ch2-swntbz.eps

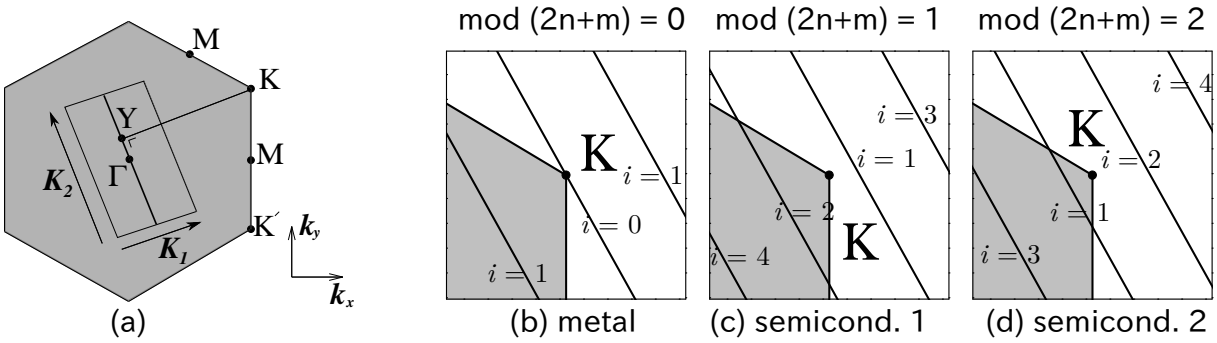

Figure 2-7: (a) The condition of metallic energy bands: if the length ratio of $|\overrightarrow{YK}|$ to $|\mathbf{K_1}|$ is an integer we get m-SWNTs otherwise we get s-SWNTs. (b), (c), and (d) illustrate of the cutting line conditions which give metallic, semiconducting type I, and semiconducting type II SWNTs respectively. Cutting line label i denotes the ascending order of cutting line distance measured from K point.

(2.34)). SWNTs energy dispersion now reads

$$E(\mathbf{k}) = E_g\left(k\frac{\mathbf{K_2}}{|\mathbf{K_2}|} + \mu\mathbf{K_1}\right), \quad \left\{\mu = -\left(\frac{N}{2} - 1\right), ..., \frac{N}{2}, \text{ and } -\frac{\pi}{T} < k < \frac{\pi}{T}\right\}, \tag{2.35}$$

where E_g is the graphene energy dispersion relation given by Eq. (2.16).

For a certain (n, m) SWNT, the absence or existence of energy gap in a SWNT depends on whether a cutting line passes through a K point of 2D graphene BZ or not. The condition for obtaining metallic energy band is that the ratio of the length of vector $\overrightarrow{YK}$ to that of $\mathbf{K_1}$ in Fig. 2-7(a) is an integer. The vector $\overrightarrow{YK}$ is given by

$$\overrightarrow{YK} = (\overrightarrow{\Gamma K} \cdot \mathbf{K_1})\frac{\mathbf{K_1}}{|\mathbf{K_1}|} = \frac{2n+m}{3}\mathbf{K_1}. \tag{2.36}$$

The modulus $\mod(2n + m, 3) = 0,\ 1,$ or 2 give metallic, semiconducting type I or type II SWNTs, respectively as shown in Fig. 2-7(b)-(d). This result implies that one-third of SWNTs are metallic while the rests are semiconducting [11].

The electronic structure of SWNTs comprise $2N$ energy bands which originate from N segments of cutting lines with each cutting line gives bonding π and anti-bonding π^* bands. Energy dispersion relation thus is plotted as a function of quasi-continuous k wave vector along $\mathbf{K_2}$. Figure 2-8(a) and (b) show the cutting lines of (4,2) s-SWNT and (15,15) m-

Fig. 2-7: fig/ch2-yk.eps

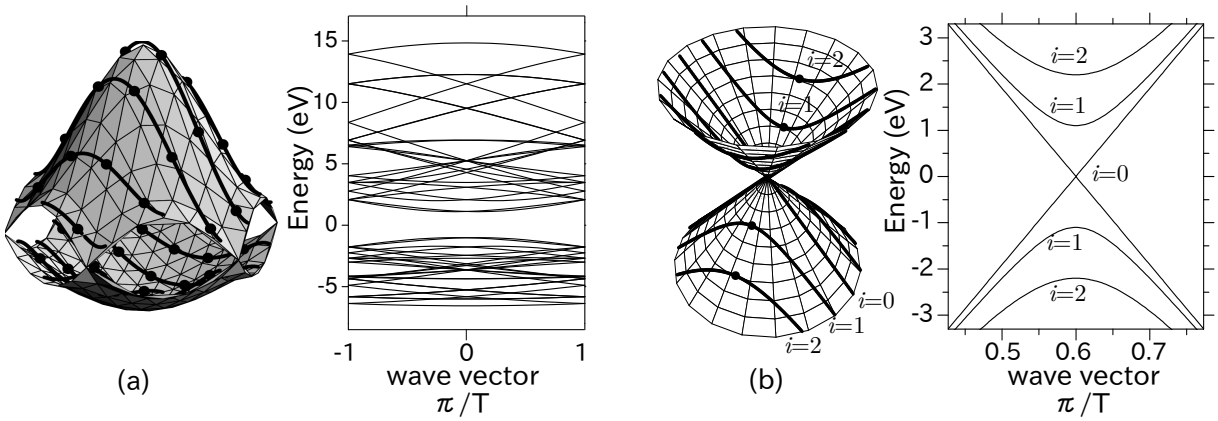

Figure 2-8: Cutting lines of (a) semiconducting (4,2) and (b) metallic (15,15) SWNTs with their corresponding energy dispersion relation. A (4,2) SWNT is a semiconducting tube since no cutting line passes through K point while (15,15) is metallic. Cutting line label i has been defined on Fig. 2-7).

SWNT with their corresponding energy dispersion.

2.1.5 Density of states of SWNTs

The electronic density of states (DOS) is defined by the number of available electronic states for a given energy interval on unit of states/1C-atom/eV. DOS determines E_{ii} values for the resonant condition for Raman spectra. DOS depends on the dimensionality of a system. Figure 2-9 depicts the dimensional dependence of DOS by nearly free electron model, which gives the parabolic energy band. In 3D system, DOS behaves as $\mathrm{DOS}(E) \propto (E - E_0)^{\frac{1}{2}}$ where E_0 is the energy minimum, in 2D system is a step-like function, in 1D system, such as SWNTs, $\mathrm{DOS}(E) \propto (E - E_0)^{-\frac{1}{2}}$ diverges at some points known as Van Hove singularity points (VHS), and finally in 0D system, DOS gives a delta function $\mathrm{DOS}(E) \propto \delta(E - E_0)$.

For given energy dispersion $E_\mu(k)$, where $\mathbf{k}$ is expressed in two numbers (μ, k) which correspond to $\mathbf{K_1}$ and $\mathbf{K_2}$ direction of a SWNT BZ respectively, DOS is given by

$$\mathrm{DOS}(E) = \frac{2}{N} \sum_{\mu=-\left(\frac{N}{2}-1\right)}^{\frac{N}{2}} \int dk \frac{1}{\left|\dfrac{dE_\mu(k)}{dk}\right|} \delta\left[E - E_\mu(k)\right]. \tag{2.37}$$

Fig. 2-8: fig/ch2-cutband.eps

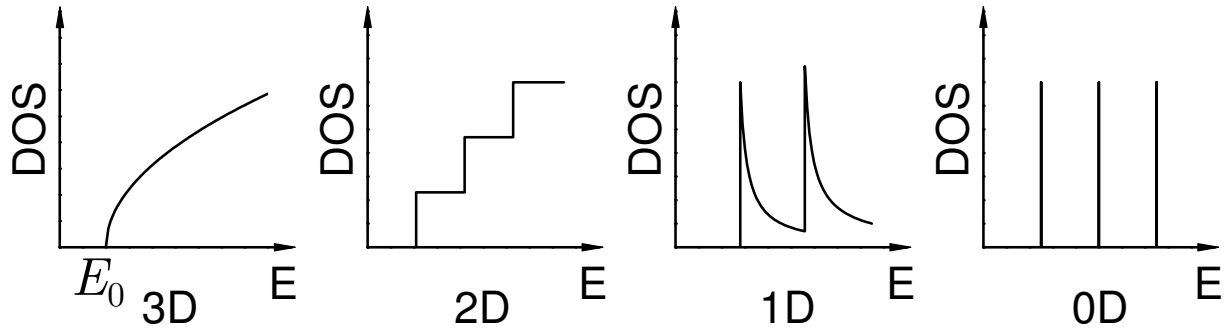

Figure 2-9: Density of states for 3D, 2D, 1D, and 0D systems.

Figure 2-10(a) and (b) shows the relationship between energy dispersion and DOS of a (9,0) SWNT. DOS gives singularities at maxima (minima) of valence (conduction) band. Around Fermi energy ($E_{\rm F} \equiv E = 0$ eV), DOS shows a finite value as what is expected linear energy band. The energy separation between two VHS arising from the i th cutting line is called transition energy E_{ii}, energy required to excite the electron from i th valence band to i th conduction band (the cutting line label i has been defined on Fig. 2-7).

The trigonal warping effect discussed in Sec. 2.1.2 induces a splitting of energy band in metallic SWNT. Figure 2-10(c) shows that even for the same distance from K point, the cutting line E_{11}^H gives higher transition energy than that of the cutting line E_{11}^L (Fig. 2-10(b)). Mapping the cutting lines on the equi-energy contour reveals that energy dispersion in $\overrightarrow{K\Gamma}$ is much steeper than that in $\overrightarrow{KM}$ direction. Thus, VHS point of cutting line E_{11}^H (E_{11}^L) which is located in $\overrightarrow{K\Gamma}$ ($\overrightarrow{KM}$) direction from K point gives a higher (lower) energy. The splitting of transition energy E_{ii} is absent in an armchair SWNT because two neighbor of the cutting lines are parallel to a $\overrightarrow{KM}$ line [34]. In a big diameter SWNT, due to the shortness of the cutting lines, E_{ii} order might exchange to each other [36].

2.1.6 Extended tight binding method

Even though STB method gives a good understanding towards electronic property of SWNTs, recent E_{ii} measurements by photoluminescence (PL) and resonance Raman spectroscopy (RRS) indicate that the STB calculation is not sufficient to interpret the experimental re-

Fig. 2-9: fig/ch2-dostypes.eps
Fig. 2-10: fig/ch2-esplit.eps

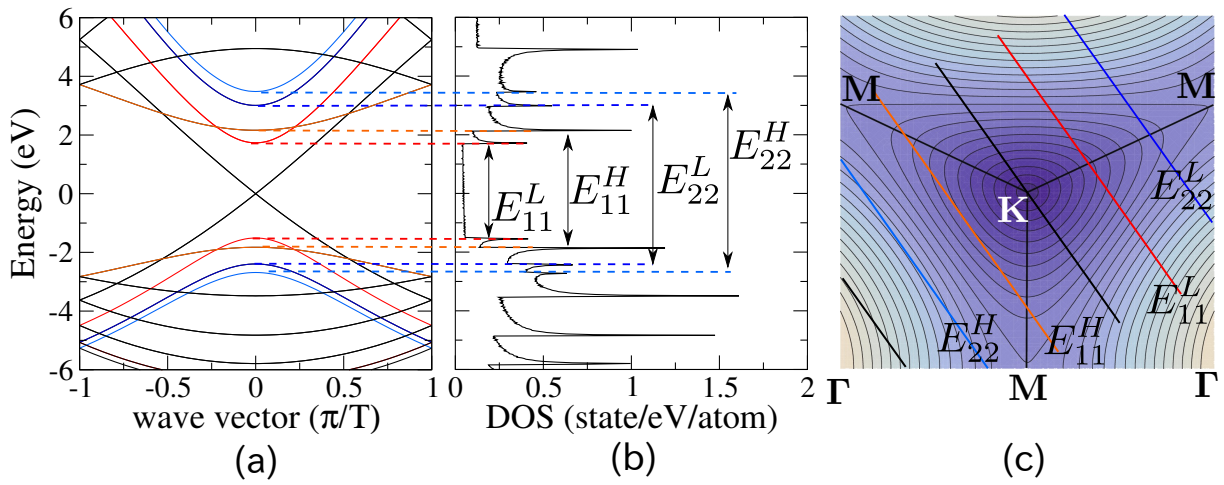

Figure 2-10: (a) Energy dispersion relation, (b) density of states, and (c) cutting lines of (9,0) SWNT in equi-energy contour which give E_{11}^L, E_{11}^H, E_{22}^L, and E_{22}^H respectively. Superscript L and H mean lower and higher, respectively.

sults [37, 38]. The experimental plot of transition energy (E_{ii}) as a function of diameter or inverse diameter (Kataura plot) in Figs. 2-11(c), (d) differs from the theoretical STB Kataura plot Fig. 2-11(a) in two different regions: in the large diameter limit and in the small diameter limit.

In the small d_t limit, the families of constant $2n + m$ deviate from the mean E_{ii} energy bands in the experimental Kataura plots, while the family spread in the theoretical Kataura plot remains relatively moderate [38]. In search for the origin of the family spread, we reconsider the limitations of the STB model discussed previously. Within the STB model, the long-range atomic interactions and the σ molecular orbitals are neglected. Meanwhile, the long-range atomic interactions are known to alternate the electronic band structure of the graphene sheet and SWNTs. On the other hand, the σ molecular orbitals are irrelevant in the graphene sheet and large diameter SWNTs as they are almost perpendicular to each other. In small diameter SWNTs, however, the curvature of the SWNTs sidewall changes the lengths of the inter-atomic bonds and the angles between them. This leads to the rehybridization of the σ and π molecular orbitals, which affects the band structure of π electrons near the Fermi level. Furthermore, the σ-π rehybridization suggests that the geometrical structure of a small diameter SWNTs deviates from the rolled up graphene sheet. A geometrical structure optimization must thus be performed to allow for atomic relaxation to equilibrium

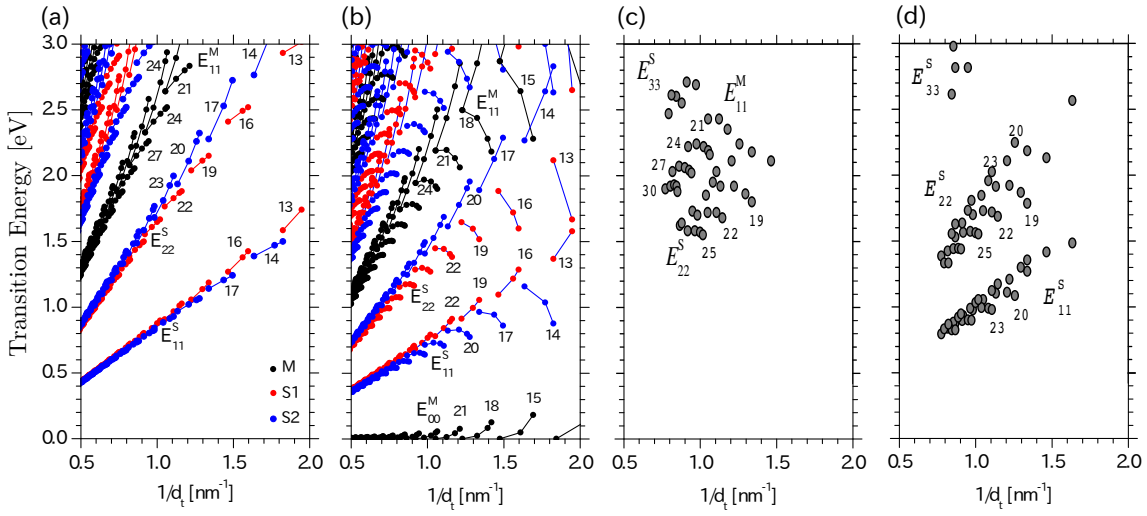

Figure 2-11: (a) The STB and (b) the ETB Kataura plot as a function of a SWNT inverse diameter $1/d_t$. The STB model only takes into account π orbital and static geometry, while the ETB model takes into account the long-range atomic interactions, the curvature effects of small diameter SWNTs, and the optimized geometrical structures of the SWNTs. Black, red, and blue dots correspond to metallic, semiconducting type I, and semiconducting type II SWNTs, respectively. The constant $2n+m$ families are connected by lines. (c) The Kataura plot extracted from resonance Raman spectroscopy [39]. (d) The Kataura plot extracted from the Photoluminiscence map [38]. The numbers show the constant $2n+m$ families.

positions. This in turn affects the E_{ii} energies of the small diameter SWNTs.

In the large d_t limit, the ratio of E_{22} to E_{11} reaches 1.8 in the experimental Kataura plots, while the same ratio goes to 2 in the STB Kataura plot [37]. The ratio problem is an indication of the many-body interactions related to the excitons, that will be discussed in Sec. 2.2.

The STB model is now extended by including the long-range atomic interactions and the σ molecular orbitals, and by optimizing the geometrical structure. The resulting model is referred to as the extended tight-binding model (ETB). Within the framework of the ETB model, we use the tight-binding parametrization determined from density-functional theory (DFT) employing the local-density approximation (LDA) and using a local orbital basis set [40]. The ETB model is discussed in detail by Samsonidze et al. [41]. The ETB Kataura plot shows a similar family spread to the PL and RRS experimental Kataura plots (see Fig. 2-11(c) and (d)). The experimental family spread is concluded to be related to

Fig. 2-11: fig/ch2-stbetb.eps

the relaxation of the geometrical structure of SWNTs. Although the family spread of the ETB model is in good agreement with the PL and RRS Kataura plots, it still deviates $200 - 300$meV from the PL and RRS experiments and the ratio problem was not solved. This deviations originates from the many-body effects or exciton effects [42].

2.2 Excitonic properties of SWNTs

2.2.1 Bethe-Salpeter equation

Exciton is an electron-hole pair bound by a Coulomb interaction and thus localized both in real space or k space. But in solids, all electrons or holes wave functions are delocalized as expressed by the Bloch wave functions. The wave vector of an electron ($\mathbf{k}_c$) or a hole ($\mathbf{k}_v$) is no longer a good quantum number in the presence of the Coulomb interaction. To create an exciton wave function from the electron and hole wave functions, the electron and hole Bloch functions at many ($\mathbf{k}_c$) and ($\mathbf{k}_v$) wave vectors have to be mixed to one another. The exciton wave function, with a center-of-mass momentum $\bar{\mathbf{K}}$ and a relative momentum $\mathbf{k}$, is a superposition of free e-h two-body states $|\mathbf{k}_{\rm c}, (\mathbf{k}-\bar{\mathbf{K}})_{\rm v}\rangle$ (Eq. (2.4)) as:

$$|\Psi^n_{\bar{\mathbf{K}}}\rangle = \sum_{\mathbf{k}} \sum_{\rm c,v} Z^n_{\mathbf{k}_{\rm c},(\mathbf{k}-\bar{\mathbf{K}})_{\rm v}} |\mathbf{k}_{\rm c}, (\mathbf{k}-\bar{\mathbf{K}})_{\rm v}\rangle. \tag{2.38}$$

The eigen vector $Z^n_{\mathbf{k}_{\rm c},(\mathbf{k}-\bar{\mathbf{K}})_{\rm v}}$ is evaluated by solving one-body Hamiltonian plus the Coulomb interaction between electron and hole, known as, Bethe—Salpeter (BS) equation [43, 44, 42]:

$$\left[E_{\mathbf{k}_{\rm c}} - E_{(\mathbf{k}-\bar{\mathbf{K}})_{\rm v}} + \sum_{\mathbf{k}'} K_{\mathbf{k}'_{\rm c}(\mathbf{k}'-\bar{\mathbf{K}})_{\rm v},\mathbf{k}_c(\mathbf{k}-\bar{\mathbf{K}})_{\rm v}} \right] Z^n_{\mathbf{k}'_{\rm c},(\mathbf{k}'-\bar{\mathbf{K}})_{\rm v}} = \Omega^n_{\bar{\mathbf{K}}} Z^n_{\mathbf{k}'_{\rm c},(\mathbf{k}'-\bar{\mathbf{K}})_{\rm v}}, \tag{2.39}$$

where $E_{\mathbf{k}_c}$ and $E_{\mathbf{k}_v}$ are the quasi-electron and quasi-hole energies, respectively. The "quasi-particle" means that many body Coulomb interactions are added to the single particle energy and the particle has a finite life time in an excited state. $\Omega^n(\bar{\mathbf{K}})$ is the n-th excited state exciton energy.

The kernel $K_{\mathbf{k}'_c\mathbf{k}'_v,\mathbf{k}_c\mathbf{k}_v}$ is given by

$$K_{\mathbf{k}'_c\mathbf{k}'_v,\mathbf{k}_c\mathbf{k}_v} = 2\delta_S K^{\mathrm{x}}_{\mathbf{k}'_c\mathbf{k}'_v,\mathbf{k}_c\mathbf{k}_v} - K^{\mathrm{d}}_{\mathbf{k}'_c\mathbf{k}'_v,\mathbf{k}_c\mathbf{k}_v}, \tag{2.40}$$

with $\delta_S = 0$ for spin triplet states and $\delta_S = 1$ for spin singlet states. The direct interaction kernel K^{d} for the screened Coulomb potential w is given by the integral

$$\begin{aligned} K^{\mathrm{d}}_{\mathbf{k}'_c\mathbf{k}'_v,\mathbf{k}_c\mathbf{k}_v} &= W_{\mathbf{k}'_c\mathbf{k}_c,\mathbf{k}'_v\mathbf{k}_v} \\ &= \int d\mathbf{r}'d\mathbf{r}\psi^*_{\mathbf{k}'_c}(\mathbf{r}')\psi_{\mathbf{k}_c}(\mathbf{r}')w(\mathbf{r}',\mathbf{r})\psi_{\mathbf{k}'_v}(\mathbf{r})\psi^*_{\mathbf{k}_v}(\mathbf{r}), \end{aligned} \tag{2.41}$$

and the exchange interaction kernel K^{x} for the bare Coulomb potential v is

$$K^{\mathrm{x}}_{\mathbf{k}'_c\mathbf{k}'_v,\mathbf{k}_c\mathbf{k}_v} = \int d\mathbf{r}'d\mathbf{r}\psi^*_{\mathbf{k}'_c}(\mathbf{r}')\psi_{\mathbf{k}'_v}(\mathbf{r}')v(\mathbf{r}',\mathbf{r})\psi_{\mathbf{k}_c}(\mathbf{r})\psi^*_{\mathbf{k}_v}(\mathbf{r}), \tag{2.42}$$

where ψ is the single particle wave function in Eq. (2.4).

The quasi-particle energies are calculated from the single particle energy $\epsilon_{\mathrm{sp}}(\mathbf{k})$ by including the self-energy corrections $\Sigma(\mathbf{k})$:

$$E_{\mathbf{k}_\mathrm{c}} = \epsilon_{\mathrm{sp}}(\mathbf{k}_c) + \Sigma(\mathbf{k}_c), \tag{2.43}$$

$$E_{\mathbf{k}_\mathrm{v}} = \epsilon_{\mathrm{sp}}(\mathbf{k}_v) + \Sigma(\mathbf{k}_v), \tag{2.44}$$

where $\Sigma(\mathbf{k})$ is expressed as

$$\Sigma(\mathbf{k}_c) = -\sum_{\mathbf{q}} W_{\mathbf{k}_c(\mathbf{k}+\mathbf{q})_v,(\mathbf{k}+\mathbf{q})_v\mathbf{k}_c}, \tag{2.45}$$

$$\Sigma(\mathbf{k}_v) = -\sum_{\mathbf{q}} W_{\mathbf{k}_v(\mathbf{k}+\mathbf{q})_v,(\mathbf{k}+\mathbf{q})_v\mathbf{k}_v}. \tag{2.46}$$

The dielectric screening effect is considered within a random phase approximation (RPA), in which the static screened Coulomb interaction is given by

$$W = \frac{V}{\kappa\epsilon(\mathbf{q})}, \tag{2.47}$$

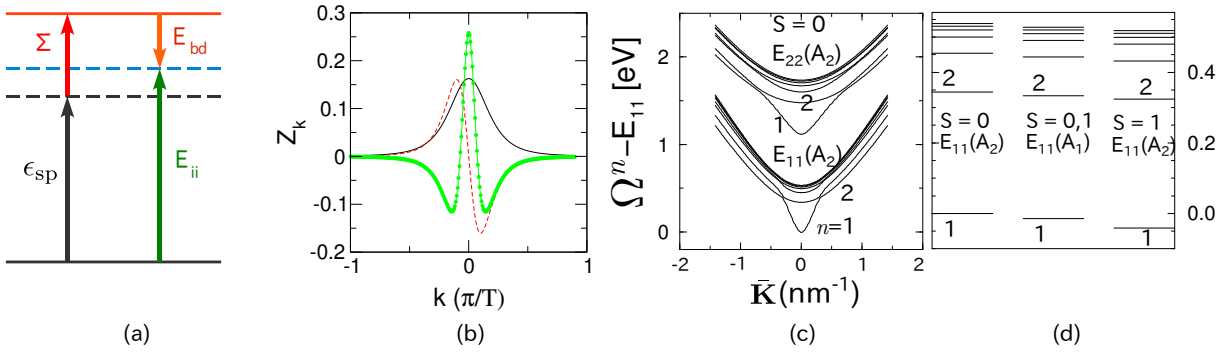

Figure 2-12: (a) The ilustration of renormalized transition energy $E_{ii} = \epsilon_{\rm sp} + \Sigma - E_{\rm bd}$ (b) The solution of the Bethe-Salpeter equation (Eq. (2.39)) which describes the first- three exciton wave states of a (8,0) SWNT. The black solid line, the red dash line, and the green dotted line show exciton state for $n = 1,\ 2,$ and 3 respectively. (c) Energy levels of singlet exciton ($S = 0$) at E_{11} and E_{22} for a (8,0) SWNT. (d) Comparison of energy state at $\bar{\mathbf{K}} = 0$ for singlet ($S = 0$) and triplet ($S = 1$) states with A_1 and A_2 symmetry.

with the dielectric function $\epsilon(\mathbf{q}) = 1 + v(\mathbf{q})\Pi(\mathbf{q})$ that describes effects of the polarization of the π bands. The effect of electrons in core states, σ bonds, and the surrounding materials are all represented by a static dielectric constant $\kappa = 2.2$. By calculating the polarization function $\Pi(\mathbf{q})$ and the Fourier transformation of the unscreened Coulomb potential $v(\mathbf{q})$, the exciton energy calculation can be performed. For 1D materials, the Ohno potential is commonly used for the unscreened Coulomb potential $v(\mathbf{q})$ for π orbitals [23].

Using the information from Eqs. (2.40)-(2.47), we can solve the BS equation (Eq. (2.39)). The solution of exciton wave function for first-three exciton states are shown in Fig.2-12(a). The exciton states comprise even and odd function along the $\mathbf{k}$ points in the cutting line. The lowest exciton state, shows a Gaussian function which indicates that exciton is localized both in reciprocal space and in real space. This localized nature of exciton is due to a strong Coulomb interaction between electron and hole in a 1D material like a SWNT.

Exciton energy dispersion is shown in Fig. 2-12 (b). Exciton energy states show discrete levels in lower energy states and continuum level in higher state. The discrete states represent bound-states of electron-hole similar to the case of Hydrogen atom.

After obtaining the excitation energy $\Omega^n(\bar{\mathbf{K}})$, the exciton binding binding energy $E_{\rm bd}$ can

Fig. 2-12: fig/ch2-excitonwf.eps

be calculated by subtracting the quasi particle energy $E_{\rm QP} = E_c(\mathbf{k}_c) - E_v(\mathbf{k}_v)$ with $\Omega^1(0)$,

$$E_{\rm bd} = E_{\rm QP} - \Omega^1(0). \tag{2.48}$$

Here $\Omega^1(0)$, which is the first (lowest) exciton state, is interpreted as the photo absorption energy E_{ii}, where an electron and a hole lie on the same $\mathbf{k}$ point of the 1D Brillouin zone of graphene. The difference between E_{ii} and the single particle band gap gives the many-body corrections $E_{\rm mb}$ which is also the difference between Σ and $E_{\rm bd}$,

$$E_{\rm mb} = \Sigma - E_{\rm bd}. \tag{2.49}$$

2.2.2 Symmetry of exciton in SWNTs

As shown in Fig. 2-13, there are three inequivalent regions in the two-dimensional Brillouin zone (2D BZ) of graphite, i.e., two triangle regions around K, K′ and one hexagonal region around the Γ point. In the case of SWNTs, the allowed wavevectors are on the so called cutting lines [35, 45] and can be expressed by $\mathbf{k} = \mu\mathbf{K}_1 + k\mathbf{K}_2/|\mathbf{K}_2|$ in Eq (2.34) [46]. Here $\mathbf{K}_1$ and $\mathbf{K}_2$ are, respectively, the reciprocal lattice vectors along the circumferential and axial directions (Eq. (2.33)). The cutting line index (integer μ) and the 1D wavevectors (k) are confined to lie within the parallelogram in Fig. 2-13. Figure 2-13 shows that the cutting lines of a SWNT are also distributed in the three inequivalent regions.

The excitons in SWNTs can then be classified according to the $2\bar{\mathbf{K}}$ in these three different regions. The optical transitions will be related to the electron and hole in the K or K′ regions. If both the electron ($\mathbf{k}_{\rm c}$) and hole ($\mathbf{k}_{\rm v}$) are from the K (or K′) region, then $2\bar{\mathbf{K}} = \mathbf{k}_{\rm c} - \mathbf{k}_{\rm v}$ lies in the Γ region and the corresponding exciton is an A symmetry exciton. If an electron is from the K region and a hole is from the K′ region, $2\bar{\mathbf{K}}$ lies in the K region and this exciton is an E symmetry exciton. If an electron is from the K region and a hole is from the K′ region, $2\bar{\mathbf{K}}$ lies in the K′ region and this exciton is an E^* symmetry exciton.

For A excitons, the electron-hole pair $|\mathbf{k}_{\rm c}, \mathbf{k}_{\rm v}\rangle = |\mathbf{k}, \bar{\mathbf{K}}\rangle$ with the electron and hole from the K region, and $|-\mathbf{k}_{\rm v}, -\mathbf{k}_{\rm c}\rangle = |-\mathbf{k}, \bar{\mathbf{K}}\rangle$ with the electron and hole from the K′ region

Fig. 2-13: fig/ch2-bz.eps

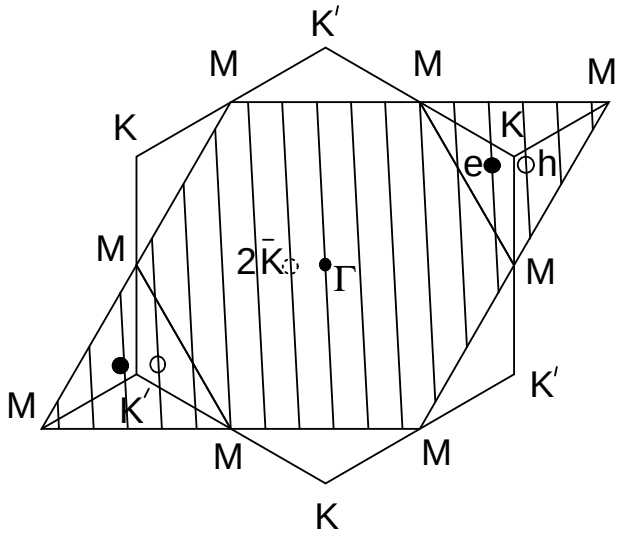

Figure 2-13: The three inequivalent regions in the 2D BZ of graphite. The cutting lines for a (6,5) SWNT are shown. The electron-hole pairs and the corresponding center-of-mass momentum $2\bar{\mathbf{K}} = \mathbf{k}_c - \mathbf{k}_v$ for an A_{12} exciton of the (6,5) SWNT are indicated. The electron-hole pair with the electron and hole lie on the second and first cutting lines to the K point and the electron-hole pair with the electron and hole lie on the first and second cutting lines to the K′ point correspond to an A_{12} exciton with the center-of-mass momentum $2\bar{\mathbf{K}}$ on the first cutting line to the Γ point.

have the same $\bar{\mathbf{K}}$. Thus, we can recombine these two electron-hole pairs to get

$$A_{2,1} = |\mathbf{k}, \pm, \bar{\mathbf{K}}\rangle = \frac{1}{\sqrt{2}}(|\mathbf{k}, \bar{\mathbf{K}}\rangle \pm |-\mathbf{k}, \bar{\mathbf{K}}\rangle). \tag{2.50}$$

Here $|\mathbf{k}, +, \mathbf{K}\rangle$ and $|\mathbf{k}, -, \mathbf{K}\rangle$ are antisymmetric and symmetric, respectively, under the C_2 (180°) rotation around the axis perpendicular to the nanotube axis. The corresponding excitons have A antisymmetric and symmetric under the C_2 rotation and are labeled as A_2 and A_1 excitons, respectively.

Because of the wave function symmetry, A_1 and A_2 states shows different energy level (Fig. 2-12(c)). In case of A_2 exciton, triplet exciton state ($S = 1$) has lower energy compared to singlet states $S = 0$ due to the correction of exchange interaction in Eq. (2.39). In the case of A_1 exciton, spin degeneracy disappears due to wave function even-symmetry in K and K′ points.

Among all of the exciton symmetry, only A_2 exciton can absorb and emit light (bright exciton). In this thesis (Sec. 3.2), we deals with A_2 exciton with $\bar{\mathbf{K}} = 0$ since the wavevector

of light is very small in comparison to graphene Brillouin zone. E and E^* excitons are dark exciton since electron and hole cannot recombine and emit photon, they possess a large $\bar{\mathbf{K}}$ while the photon wave vector is almost negligible. A_1 exciton is also dark exciton because of the vanishing exciton-photon matrix element (see Appendix A.1)

2.2.3 Exciton effect in SWNTs

To understand how significant exciton effect in the photo-absorption process in SWNTs, we present a Kataura plot of $E_{\rm bd}$ for some m-SWNTs and s-SWNTs in Fig. 2-14(a) and (b). Exciton binding energy is calculated within STB method by Jiang et al. [42]. From this calculation we found that $E_{\rm bd}$ in s-SWNTs are around ~ 0.3 eV for $d_t \approx 2$ nm and increase to ~ 1 eV as $d_t \approx 0.5$ nm. This d_t dependence of $E_{\rm bd}$ come from the fact that the Coulomb interaction is proportional to $1/d_t$. $E_{\rm bd}$ in small d_t s-SWNTs is in the same order with the single particle electron energy. Thus the renormalization of electron by considering exciton effect in SWNTs is significant. $E_{\rm bd}$ in m-SWNTs shows the same tendency with its values one-order smaller than that of s-SWNTs due to screening effect which weakened the Coulomb interaction [42].

To understand whether the single particle spectra or many-body effects contribute to the large family spread in the exciton Kataura plot, the transition energy E_{11}, the self-energy Σ, the exciton binding energy $E_{\rm bd}$, and the energy correction to the single particle energy (many-body correction) $\Sigma - E_{\rm bd}$ are plotted in the same figure (Fig. 2-14(c)). Although both Σ and $E_{\rm bd}$ tend to increase the family spread in smaller diameter SWNTs, the two values almost cancel each other regarding the family spread, leading to a weak chirality dependence. The large family spread observed in E_{ii} is thus concluded to originate from the trigonal warping effect in the single-particle spectra [34]. The net-energy correction (Σ–$E_{\rm bd}$) to the single-particle energy depends predominantly on d_t. The correction has a logarithmic nature, owing to the effect of the Coulomb interaction on the dispersion of graphene [47],

$$E_{\log} = 0.55(2p/3d_t)\log\left[3\left(\frac{3d_t}{2p}\right)\right], \tag{2.51}$$

where p is an integer corresponds to the ratio of the distances of the cutting lines for each

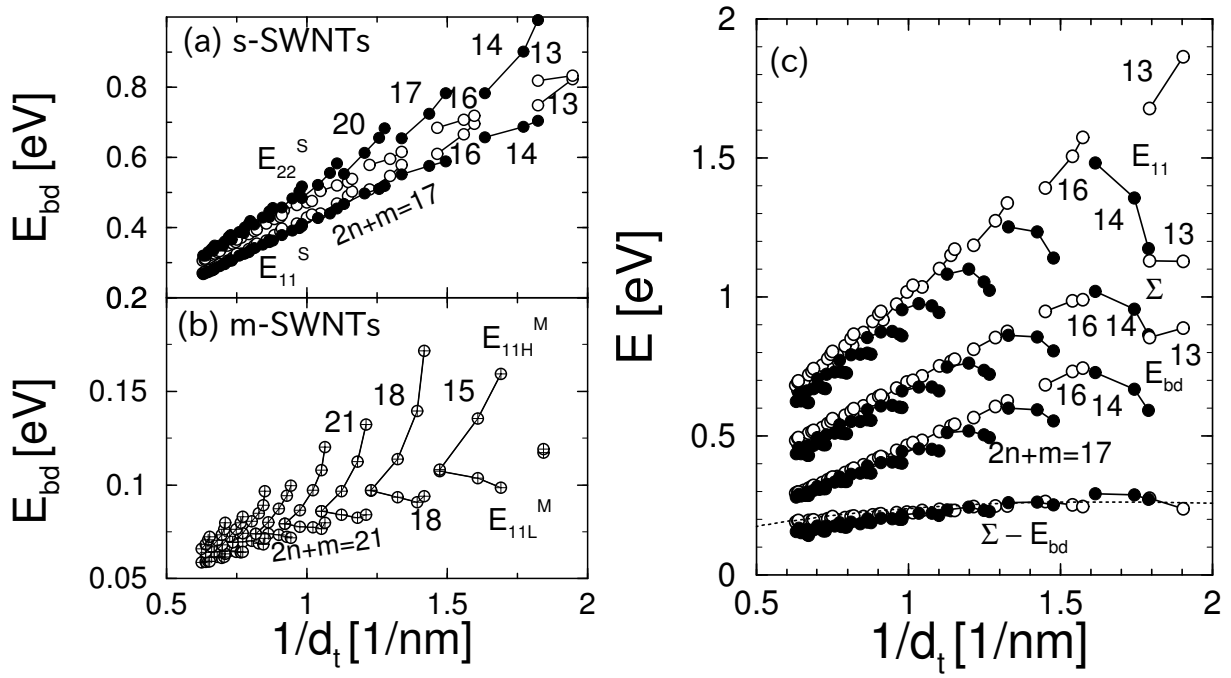

Figure 2-14: Kataura plot of exciton binding energy $E_{\rm bd}$ for (a) s-SWNTs and (b) m-SWNTs. The result is taken from Ref. [42] within STB method.(c) The excitation energy $E_{11} = \Omega_0$, self energy Σ, exciton binding energy $E_{\rm bd}$, and many body correction $E_{\rm mb}$. The dashed line is taken from Eq. (2.51) . The result is taken from Ref. [42] within ETB method.

E_{ii} transition from the K-point in 2D Brillouin zone of graphene [34], $p = 1, 2, 3, 4, 5$ stands for $E_{11}^{\rm S}$, $E_{22}^{\rm S}$, $E_{11}^{\rm M}$, $E_{33}^{\rm S}$, and $E_{44}^{\rm S}$, respectively. In Fig. 2-14(c), $E_{\log}$ with $p = 1$ is plotted as a dashed line. It can be seen that the many-body correction $\Sigma - E_{\rm bd}$ calculated in the exciton picture follows the logarithmic behavior very well. And thus, the ratio problem has been solved by considering many body correction and exciton effect.

Fig. 2-14: fig/ch2-exbdsm.eps

Chapter 3

Calculation of Raman spectra

In this Chapter we discuss the Raman scattering process which occurs in SWNTs. The ground state is defined by the states where all electrons occupy the valence band of a SWNT. Optical process starts after laser excitation energy is introduced. An exciton is thus generated as a virtual state via exciton-photon interaction. This photo-excited carrier may undergo exciton-phonon interaction or exciton-exciton interaction and then relaxes to the conduction band bottom before emitting a scattered photon by electron-hole recombination.

3.1 Raman scattering amplitudes

Depending on the number of scattering process, we define the order of Raman scattering (Fig. 3-1). First-order (second-order) scattering corresponds to one- (two-) emission of excitation(s). In this calculation, we restrict our self to take into account only up to second-order resonance Raman process. Here the resonance means that the one (two) intermediate state is real electronic states (solid dots in Fig. 3-1) for the first (second) order process. They are either incident or scattered resonance, respectively, in which incident or the scattered light has the same energy as the electronic transition energy. The first order Raman scattering

Fig. 3-1: fig/ch3-srdr.eps

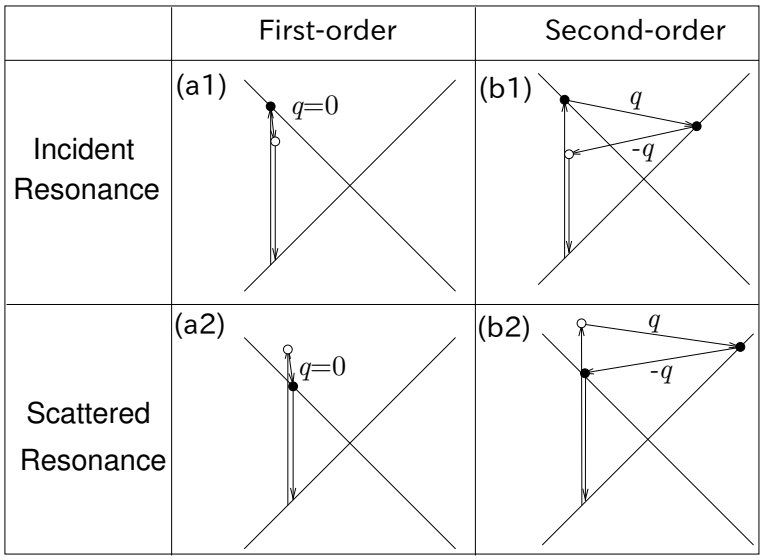

Figure 3-1: (a) First-order, and (b) second-order resonance Raman spectral processes. (top) incident photon resonance conditions and (bottom) scattered photon resonance conditions. First-order process deals with zone center ($q = 0$) excitation. Resonance points are shown as solid circles [7].

amplitude within time-dependent perturbation theory is given by:

$$A_{\nu}^{(1)}(\omega_{\rm s}) = \frac{1}{\pi}\sum_{n,n'}\left[\frac{\mathcal{M}_{\rm ex-op}^{n,i}}{[\Delta E_{ni} - i\gamma]}\frac{\mathcal{M}_{\rm ex-ph}^{n',n}}{[\Delta E_{n'i} - \hbar\omega_{\nu} - i(\gamma+\Gamma_{\nu})]}\frac{\mathcal{M}_{\rm ex-op}^{f,n'}}{[E_{\rm L} - \hbar\omega_{\nu} - \hbar\omega_{\rm s} - i\Gamma_{\nu}]}\right], \quad (3.1)$$

where ν = zone-center ($q = 0$) phonon (RBM or G) mode, and $\Delta E_{mi} = E_{\rm L} - E_m - E_i$. We use a broadening factor $\gamma = 60$ meV which is relevant to the life time of the photo-excited carriers [48]. We also utilize the phonon spectral width for the RBM as a constant $\Gamma_{\rm RBM} = 10$ cm^{-1}, and for the G band, which consist of in-plane transverse optic (iTO) $\Gamma_{\rm iTO} = 20$ cm^{-1} and longitudinal optic (LO) $\Gamma_{\rm LO} = 31$ cm^{-1} [49]. The exciton-photon ($\mathcal{M}_{\rm ex-op}^{b,a}$) and exciton-phonon ($\mathcal{M}_{\rm ex-ph}^{b,a}$) matrix elements for a transition between states $a \rightarrow b$ are calculated by Jiang's program [50]. We approximate that the final state is the same as initial state $i = f$ and the virtual states $n = n'$. Such virtual states $|\rm vir\rangle$ are generally given by linear combination of many exciton states $|n\rangle$

$$|\rm vir\rangle = \sum_{\rm n} A_{\rm n}|\rm n\rangle. \quad (3.2)$$

However, we assume that the virtual states can be considered as the lowest exciton state (see Appendix B for detailed derivation).

The second-order Raman scattering amplitude of ERS process, is given by:

$$A^{(2)}_{\mathrm{ERS}}(\omega_{\mathrm{s}}) = \frac{1}{\pi} \sum_{n,n',n'',\sigma} \left[\frac{\mathcal{M}^{n,i}_{\mathrm{ex-op}}}{[\Delta E_{ni} - i\gamma]} \frac{\mathcal{M}^{n',n}_{\mathrm{ex-ex}}(q)}{[\Delta E_{n'i} - \hbar\omega_1 - i(\gamma + \Gamma_{\mathrm{x}})]} \frac{\mathcal{M}^{n'',n'}_{\mathrm{ex-ex}}(-q)}{[\Delta E_{n''i} - \hbar\omega_1 - \hbar\omega_2 - i(\gamma + 2\Gamma_{\mathrm{x}})]} \times \frac{\mathcal{M}^{f,n'}_{\mathrm{ex-op}}}{[E_{\mathrm{L}} - \hbar\omega_1 - \hbar\omega_2 - \hbar\omega_{\mathrm{s}} - 2i\Gamma_{\mathrm{x}}]} \right], \tag{3.3}$$

where we also consider the same virtual state approximation as in Eq. (3.1). Here, ω_1 and ω_2 are the energies of the linear band excitons emitted from the exciton-exciton interaction in the second-order ERS process (Fig. 3-2(b) and (c)). The summation over σ denotes all different processes in the ERS mechanism, i.e. intra-valley and inter-valley interaction as shown in Fig 3-2(b) and (c), respectively. The electron-electron interaction life time is assumed a constant value $\Gamma_{\mathrm{x}} = 25$ meV so as to reproduce the experimental ERS spectral width [6]. The exciton-exciton matrix elements $\mathcal{M}^{n',n}_{\mathrm{ex-ex}}(q)$ are later proven in Sec. 3.3 to be negligible at $q = 0$ and thus the first order Raman process (Fig. 3-2(a)) is negligible.

The Raman intensity is calculated by the square of the sum of the RBM and G phonon amplitudes and the ERS amplitudes since they have the same initial and state which interfered to one another. Raman intensity I is given by:

$$I = \sum_i \left| \sum_f \left(A_{\mathrm{RBM}} + A_{\mathrm{G}} + A_{\mathrm{ERS}} \right) \right|^2 , \tag{3.4}$$

where $A_{\mathrm{G}} = A_{\mathrm{iTO}} + A_{\mathrm{LO}}$. We do not consider the G$'$ band (second order process of K-point iTO mode [9]) in this current study for simplicity.

In appendix A.1 and A.2 we review the work by Jiang et al. to calculate exciton-photon and exciton-phonon matrix elements within tight binding (TB) approximation [50]. While Sec. 3.2 is the present thesis original works of exciton-exciton matrix elements.

3.2 Exciton-exciton interaction

Optical processes of the ERS consist of (i) an exciton generation via an exciton-photon interaction, (ii) excitation of another exciton (s) in the linear energy band by the Coulomb interaction with the photo-excited exciton, and (iii) finally the photo-excited exciton goes back to the ground state by emitting a photon. The exciton-exciton interaction in (ii) may occur in either a first-order or high-order process. Here, we consider up to second-order processes for simplicity. For the first-order process, the photo-excited exciton relaxes vertically ($\mathbf{q} = 0$) from a virtual state $\Psi^{\rm vir}$ to the E_{ii} state after photo-absorption at a wave vector $\mathbf{k}$, while the other exciton is created in the linear band at wave vector $\mathbf{k}^{'}$ by the Coulomb interaction with $\mathbf{q} = 0$ (see Fig. 3-2(a)). In the second-order process, on the other hand, the existence of the two inequivalent K and K$'$ points in the graphene Brillouin zone leads to two different scattering processes, i.e. *intra-valley* (AV) interaction and the *inter-valley* (EV) interaction, shown in Figs. 3-2(b) and (c), respectively since the excitons at parabolic and linear bands may exist in the same valley (A state), or they may exist in the different valleys (E state). Such a symmetry labeling for A and E states is obtained from group theory [51]. After going through the electronic scattering process, the photo-excited exciton then recombine to the ground state at $\mathbf{k}$ by emitting a photon with resonance energy $E_{\rm s} = E_{ii}$. This is the reason why the ERS peak position always appear at E_{ii} even though we change the laser energy $E_{\rm L}$.

Considering each process denoted by $\rightsquigarrow$ arrows shown in Fig. 3-2, we write the perturbed Hamiltonian as:

$$H_{\rm e-e} = \sum_{\mathbf{k},\mathbf{k}',\mathbf{q}} W^{(\pm)}_{\mathbf{k}+\mathbf{q},\mathbf{k}'-\mathbf{q},\mathbf{k},\mathbf{k}'} c^{\dagger {\rm c}}_{\mathbf{k}+\mathbf{q}} c^{\dagger {\rm c}'}_{\mathbf{k}'-\mathbf{q}} c^{\rm v'}_{\mathbf{k}'} c^{\rm c}_{\mathbf{k}}, \tag{3.5}$$

where $\mathbf{k}$ and $\mathbf{k}^{'}$ denote, respectively, an electron state in the parabolic and the linear band, while $c^{\dagger {\rm c}}_{\mathbf{k}}(c^{\rm v}_{\mathbf{k}})$ is the creation (annihilation) operator in the conduction (valence) band. Here we only consider the scattering of electron and did not consider the scattering of hole for simplicity. The two-body Coulomb interaction W consists of the direct $K^{\rm d}$ and the exchange

Fig. 3-2: fig/ch3-ersprocess.eps

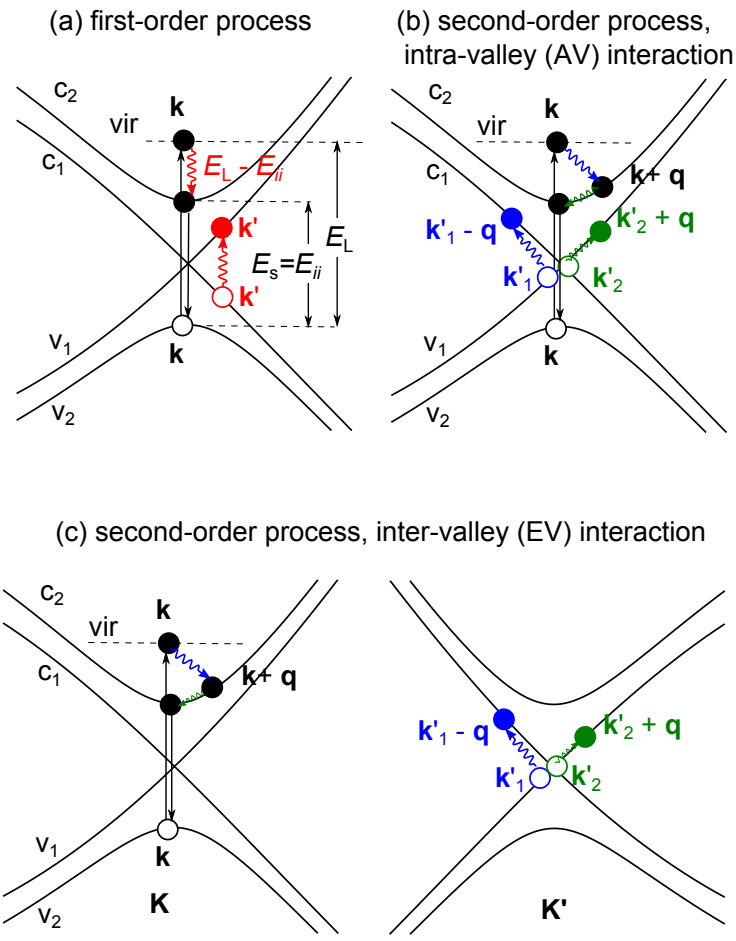

Figure 3-2: All possible (a) First-order electronic Raman process. (b) AV and (c) EV second-order scattering processes ($\mathbf{q} \neq 0$). In both the first-order and second-order processes, the interaction between electrons in the parabolic band and the linear band can take place in the same valley (K or K′ points) or in a different valley.

K^{x} interaction by following relationship: $W^{(\pm)} = K^{\mathrm{d}} \pm K^{\mathrm{x}}$, in which $+(-)$ gives a singlet (triplet) state for the two electrons. A detailed derivation for K^{d} and K^{x} will be presented in Sec. 3.3.

The exciton-exciton matrix element for the photo-excited exciton and another exciton in a linear energy band is calculated using the following formula:

$$\begin{aligned}\mathcal{M}^{\pm}_{\mathrm{ex-ex}}(\mathbf{q}) =& \langle \Psi^{f} | H_{\mathrm{e-e}} | \Psi^{\mathrm{vir}} \rangle \\ =& \sum_{\mathbf{k},\mathbf{k}'} Z^{n=0*}_{(\mathbf{k}+\mathbf{q})\mathrm{c},\mathbf{k}\mathrm{v}} Z^{n=0*}_{(\mathbf{k}'-\mathbf{q})\mathrm{c},\mathbf{k}'\mathrm{v}} Z^{n=0}_{\mathbf{k}\mathrm{c},\mathbf{k}\mathrm{v}} W^{(\pm)}_{\mathbf{k}+\mathbf{q},\mathbf{k}'-\mathbf{q},\mathbf{k},\mathbf{k}'}. \end{aligned} \tag{3.6}$$

Here the photo-excited exciton state is defined by:

$$|\Psi^{\mathrm{vir}}\rangle = \sum_{\mathbf{k}} Z^{n=0}_{\mathbf{kc},\mathbf{kv}} c^{\dagger \mathrm{c}}_{\mathbf{k}} c^{\mathrm{v}}_{\mathbf{k}} |g\rangle, \tag{3.7}$$

where $Z^{n*}_{\mathbf{k}_\mathrm{c},\mathbf{k}_\mathrm{v}}$ is the eigenvector of the $n-$th exciton state solved from the Bethe-Salpeter equation (Eq. (2.39)), $\mathbf{k}_c$ and $\mathbf{k}_\mathrm{v}$ denote wave vectors for the electron and hole states, respectively, with $\mathbf{k}_c = \mathbf{k}_\mathrm{v}$ for a bright exciton (see Sec. 2.2.2), and $|g\rangle$ denotes the ground state [42]. In Eq. (3.7), we only use the lowest exciton state $n = 0$, since it gives the dominant contribution to the Raman spectra (see Appendix B).The final state of Eq. (3.6) is given by:

$$|\Psi^{f}\rangle = \sum_{\mathbf{k},\mathbf{k}'} Z^{n=0}_{(\mathbf{k}+\mathbf{q})\mathrm{c},\mathbf{kv}} Z^{n=0}_{\left(\mathbf{k}'-\mathbf{q}\right)\mathrm{c},\mathbf{k}'\mathrm{v}} c^{\dagger \mathrm{c}}_{\mathbf{k}+\mathbf{q}} c^{\dagger \mathrm{c}}_{\mathbf{k}'-\mathbf{q}} c^{\mathrm{v}}_{\mathbf{k}'} c^{\mathrm{v}}_{\mathbf{k}} |g\rangle. \tag{3.8}$$

3.3 Electron-electron interaction

In this section we elaborate the calculation of electron-electron interaction $W^{(\pm)}_{\mathbf{k}+\mathbf{q},\mathbf{k}'-\mathbf{q},\mathbf{k},\mathbf{k}'}$ within tight binding (TB) approximation. An important conclusion of this section is that for the electron-electron interaction between the photo-excited and the linear band excitons, the direct interaction K^{d} vanishes at $\mathbf{q} = 0$ (and thus the exciton-exciton matrix element for the direct interaction becomes also zero). This is not due to the exciton effect but simply comes about because of symmetry of the A and B sublattice in graphene unit cell. The direct interaction K^{d} already vanishes at $\mathbf{q} = 0$ by considering the symmetry of the A and B sublattices, before taking into account the summation on $\mathbf{k}$ weighted by the exciton wave function $Z_{\mathbf{k}}$ (Eq. (3.6)). The interaction between an electron in the parabolic-band and an electron in the linear band of a metallic single wall carbon nanotube (m-SWNT) without the screening effect is given by

$$V\left(\mathbf{k_1}a_1, \mathbf{k_2}a_2, \mathbf{k_3}a_3, \mathbf{k_4}a_4\right)^{(\pm)} = \int d\mathbf{r}d\mathbf{r}'\Phi^{\mathrm{f}*(\pm)}(\mathbf{r},\mathbf{r}')v\left(\mathbf{r},\mathbf{r}'\right)\Phi^{\mathrm{vir}(\pm)}(\mathbf{r},\mathbf{r}'), \tag{3.9}$$

where $(\mathbf{k_1}a_1, \mathbf{k_2}a_2, \mathbf{k_3}a_3, \mathbf{k_4}a_4) \equiv \left\{\left(\mathbf{k}+\mathbf{q}\right)_\mathrm{c}, \left(\mathbf{k}'-\mathbf{q}\right)_\mathrm{c}, \mathbf{k}_\mathrm{c}, \mathbf{k}'_\mathrm{v}\right\}$ in Eq. (3.5), a_i denotes either c (conduction) or v (valence) band states, and $\mathbf{k}$ ($\mathbf{k}'$) is a wave vector for the parabolic (linear) band. Φ^{vir} and Φ^{f} are the final and virtual states of two interacting electrons. The two-body

wave function of electrons at the parabolic band and linear band in the virtual state $\Phi^{\rm vir}$ is defined as:

$$\Phi^{\rm vir(\pm)}(\mathbf{r},\mathbf{r}') = \frac{1}{\sqrt{2}}\left[\psi_{\mathbf{k3}a3}(\mathbf{r})\,\psi_{\mathbf{k4}a4}(\mathbf{r}') \pm \psi_{\mathbf{k3}a3}(\mathbf{r}')\,\psi_{\mathbf{k4}a4}(\mathbf{r})\right], \tag{3.10}$$

and the final state $\Phi^{\rm f}$ is defined as:

$$\Phi^{\rm f(\pm)}(\mathbf{r},\mathbf{r}') = \frac{1}{\sqrt{2}}\left[\psi_{\mathbf{k1}a1}(\mathbf{r})\,\psi_{\mathbf{k2}a2}(\mathbf{r}') \pm \psi_{\mathbf{k1}a1}(\mathbf{r}')\,\psi_{\mathbf{k2}a2}(\mathbf{r})\right], \tag{3.11}$$

where the $+\,(-)$ sign is taken for the spin singlet (triplet) state. Here we do not explicitly show spins functions for simplicity since the Coulomb interaction does not change the spin direction. $\psi_{\mathbf{k}a}(\mathbf{r})$ is a one-electron wavefunction specified by wave vector $\mathbf{k}$, subband $a =$ c, v, and position $\mathbf{r}$.

Substituting Eqs. (3.10) and (3.11) into Eq. (3.9) we obtain

$$V(\mathbf{k_1}a_1,\mathbf{k_2}a_2,\mathbf{k_3}a_3,\mathbf{k_4}a_4)^{(\pm)} = K^{\rm d} \pm K^{\rm x}, \tag{3.12}$$

where the direct interaction $K^{\rm d}$ and exchange interaction $K^{\rm x}$ terms are expressed by

$$K^{\rm d} = \frac{1}{2}\left\{K(\mathbf{k_1}a_1,\mathbf{k_2}a_2,\mathbf{k_3}a_3,\mathbf{k_4}a_4) + K(\mathbf{k_2}a_2,\mathbf{k_1}a_1,\mathbf{k_4}a_4,\mathbf{k_3}a_3)\right\}, \tag{3.13}$$

$$K^{\rm x} = \frac{1}{2}\left\{K(\mathbf{k_1}a_1,\mathbf{k_2}a_2,\mathbf{k_4}a_4,\mathbf{k_3}a_3) + K(\mathbf{k_2}a_2,\mathbf{k_1}a_1,\mathbf{k_3}a_3,\mathbf{k_4}a_4)\right\}, \tag{3.14}$$

and the Coulomb integral K is defined by

$$K(\mathbf{k_1}a_1,\mathbf{k_2}a_2,\mathbf{k_3}a_3,\mathbf{k_4}a_4) = \int d\mathbf{r}d\mathbf{r}' v(\mathbf{r},\mathbf{r}')\,\psi^*_{\mathbf{k1}a1}(\mathbf{r})\,\psi^*_{\mathbf{k2}a2}(\mathbf{r}')\,\psi_{\mathbf{k3}a3}(\mathbf{r})\,\psi_{\mathbf{k4}a4}(\mathbf{r}'). \tag{3.15}$$

The one-electron wave function $\psi_{\mathbf{k}}$ can be explicitly written by the TB wave function Eq. (2.4)

$$\psi_{\mathbf{k}a}(\mathbf{r}) = \frac{1}{\sqrt{N_{\rm u}}}\sum_{s=A,B}\sum_{u=1}^{N_u} C_s^a(\mathbf{k})\,e^{i\mathbf{k}.\mathbf{R}_{us}}\varphi(\mathbf{r}-\mathbf{R}_{us}), \tag{3.16}$$

where $N_{\rm u}$ is the number of hexagons in a SWNT unit cell, $\mathbf{R}$ is the atomic position, and $\varphi(\mathbf{r}-\mathbf{R})$ is the atomic orbital at $\mathbf{R}$. The TB coefficient $C_s^a(\mathbf{k})$ has been derived in Eq. (2.24),

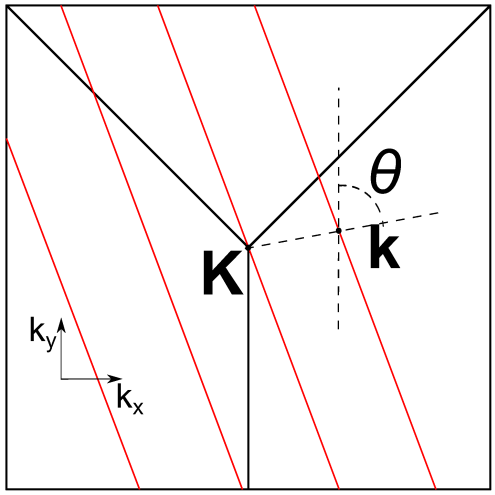

Figure 3-3: The phase factor θ in Eq. (3.17) is defined by the smallest angle between k_y axis and a line passing through a $\mathbf{k}$ point measured from the K (or K') point, and therefore $\theta = \arctan(k_x/k_y)$.

and choosing the phase factor ($\phi_{\rm c} = \phi_{\rm v} = -\theta(\mathbf{k})/2$) so as to get

$$\begin{aligned} C_A^c(\mathbf{K}+\mathbf{k}) &= \frac{1}{\sqrt{2}} e^{-i\theta(\mathbf{k})/2}, \quad C_B^c(\mathbf{K}+\mathbf{k}) = \frac{1}{\sqrt{2}} e^{+i\theta(\mathbf{k})/2}, \\ C_A^v(\mathbf{K}+\mathbf{k}) &= \frac{1}{\sqrt{2}} e^{-i\theta(\mathbf{k})/2}, \quad C_B^v(\mathbf{K}+\mathbf{k}) = -\frac{1}{\sqrt{2}} e^{+i\theta(\mathbf{k})/2}, \end{aligned} \tag{3.17}$$

where $\theta = \arctan(k_x/k_y)$ measured from the K or K$'$ points (see Fig.3-3, vectors corresponding to the K and K$'$ points are denoted $\mathbf{K}$ and $\mathbf{K}'$, respectively) [52]. In Eq. (3.17), we have set the overlap integral $s = 0$ (Eq. (2.24)). The TB coefficient near K$'$ point can be obtain by taking complex conjugate of corresponding coefficient near K point.

Fig. 3-3: ch3-theta.eps

Substituting Eq. (3.16) into Eq. (3.15), we get

$$
\begin{aligned}
& K(\mathbf{k_1}a_1, \mathbf{k_2}a_2, \mathbf{k_3}a_3, \mathbf{k_4}a_4) \qquad (3.18)\\
=& \frac{1}{N_u^2} \sum_{s_1 u_1, s_2 u_2} \Bigg[\sum_{s_1' u_1', s_2' u_2'} C_{s_1}^{a_1 *}(\mathbf{k}_1)\, e^{-i\mathbf{k_1}.\mathbf{R}_{u_1 s_1}} C_{s_1'}^{a_2 *}(\mathbf{k}_2)\, e^{-i\mathbf{k_2}.\mathbf{R}_{u_1' s_1'}} \\
& \times C_{s_2}^{a_3}(\mathbf{k}_3)\, e^{i\mathbf{k_3}.\mathbf{R}_{u_2 s_2}} C_{s_2'}^{a_4}(\mathbf{k}_4)\, e^{i\mathbf{k_4}.\mathbf{R}_{u_2' s_2'}} \\
& \times \int d\mathbf{r} d\mathbf{r}' v(\mathbf{r}, \mathbf{r}')\, \varphi(\mathbf{r} - \mathbf{R}_{u_1 s_1})\, \varphi\left(\mathbf{r}' - \mathbf{R}_{u_1' s_1'}\right) \varphi(\mathbf{r} - \mathbf{R}_{u_2 s_2})\, \varphi\left(\mathbf{r}' - \mathbf{R}_{u_2' s_2'}\right) \Bigg]. \qquad (3.19)
\end{aligned}
$$

The largest contribution from the integrand comes from $(u_1 s_1) = (u_2 s_2) \equiv (us)$ and $(u_1' s_1') = (u_2' s_2') \equiv (u's')$. Thus Eq. (3.18) becomes

$$
\begin{aligned}
K(\mathbf{k_1}a_1, \mathbf{k_2}a_2, \mathbf{k_3}a_3, \mathbf{k_4}a_4) &\cong \frac{1}{N_u^2} \sum_{su} \sum_{s'u'} C_s^{a_1 *}(\mathbf{k}_1)\, C_{s'}^{a_2 *}(\mathbf{k}_2)\, C_s^{a_3}(\mathbf{k}_3)\, C_{s'}^{a_4}(\mathbf{k}_4) \\
&\quad \times e^{-i\mathbf{k_1}.\mathbf{R}_{us}} e^{-i\mathbf{k_2}.\mathbf{R}_{u's'}} e^{i\mathbf{k_3}.\mathbf{R}_{us}} e^{i\mathbf{k_4}.\mathbf{R}_{u's'}} \\
&\quad \times \int d\mathbf{r} d\mathbf{r}' v(\mathbf{r}, \mathbf{r}') \left|\varphi(\mathbf{r} - \mathbf{R}_{us})\right|^2 \left|\varphi(\mathbf{r}' - \mathbf{R}_{u's'})\right|^2 \\
&= \frac{1}{N_u^2} \sum_{su} \sum_{s'u'} C_s^{a_1 *}(\mathbf{k}_1)\, C_{s'}^{a_2 *}(\mathbf{k}_2)\, C_s^{a_3}(\mathbf{k}_3)\, C_{s'}^{a_4}(\mathbf{k}_4) \\
&\quad \times e^{i(\mathbf{k_3} - \mathbf{k_1}).\mathbf{R}_{us}} e^{i(\mathbf{k_4} - \mathbf{k_2}).\mathbf{R}_{u's'}} \\
&\quad \times \int d\mathbf{r} d\mathbf{r}' v(\mathbf{r}, \mathbf{r}') \left|\varphi(\mathbf{r} - \mathbf{R}_{us})\right|^2 \left|\varphi(\mathbf{r}' - \mathbf{R}_{u's'})\right|^2 \\
&= \frac{1}{N_u^2} \sum_{su} \sum_{s'u'} C_s^{a_1 *}(\mathbf{k}_1)\, C_{s'}^{a_2 *}(\mathbf{k}_2)\, C_s^{a_3}(\mathbf{k}_3)\, C_{s'}^{a_4}(\mathbf{k}_4) \\
&\quad e^{i(\mathbf{k_3} - \mathbf{k_1} + \mathbf{k_4} - \mathbf{k_2}).\mathbf{R}_{us}} e^{i(\mathbf{k_4} - \mathbf{k_2}).(\mathbf{R}_{u's'} - \mathbf{R}_{us})} \\
&\quad \times \int d\mathbf{r} d\mathbf{r}' v(\mathbf{r}, \mathbf{r}') \left|\varphi(\mathbf{r} - \mathbf{R}_{us})\right|^2 \left|\varphi(\mathbf{r}' - \mathbf{R}_{u's'})\right|^2 .
\end{aligned}
$$

By using the fact that $\sum_{u,s} e^{i(\mathbf{k_3} - \mathbf{k_1} + \mathbf{k_4} - \mathbf{k_2}).\mathbf{R}_{us}} = N_u \delta(\mathbf{k_3} + \mathbf{k_4}, \mathbf{k_1} + \mathbf{k_2})$, we get

$$
\begin{aligned}
K(\mathbf{k_1}a_1, \mathbf{k_2}a_2, \mathbf{k_3}a_3, \mathbf{k_4}a_4) &= \sum_{ss'} C_s^{a_1 *}(\mathbf{k}_1)\, C_{s'}^{a_2 *}(\mathbf{k}_2)\, C_s^{a_3}(\mathbf{k}_3)\, C_{s'}^{a_4}(\mathbf{k}_4)\, v_{ss'}(\mathbf{k_4} - \mathbf{k_2}) \\
&\quad \times \delta(\mathbf{k_3} + \mathbf{k_4}, \mathbf{k_1} + \mathbf{k_2}), \qquad (3.20)
\end{aligned}
$$

where

$$v_{ss'}(\mathbf{q}) = \frac{1}{N_u}\sum_{u'} e^{i\mathbf{q}\cdot(\mathbf{R}_{u's'}-\mathbf{R}_{0s})}\int d\mathbf{r}d\mathbf{r}' v(\mathbf{r},\mathbf{r}')\left|\varphi(\mathbf{r}-\mathbf{R}_{0s})\right|^2\left|\varphi(\mathbf{r}'-\mathbf{R}_{u's'})\right|^2, \tag{3.21}$$

is the Fourier transform of the Coulomb integral. When we define the integration of Eq. (3.21) as $v(\mathbf{R}_{0s},\mathbf{R}_{u's'})$,

$$v_{ss'}(\mathbf{q}) = \frac{1}{N_u}\sum_{u'} e^{i\mathbf{q}\cdot(\mathbf{R}_{u's'}-\mathbf{R}_{0s})} v(\mathbf{R}_{0s},\mathbf{R}_{u's'}), \tag{3.22}$$

we can show that $v_{\mathrm{AA}}(\mathbf{q}) = v_{\mathrm{BB}}(\mathbf{q})$ and $v_{\mathrm{AB}}(\mathbf{q}) = v^*_{\mathrm{BA}}(\mathbf{q})$ because of the symmetry between A and B sublattices. The Coulomb potential $v(\mathbf{R},\mathbf{R}')$ for the π electron system is modeled by the Ohno potential [42, 53, 54]:

$$v(\mathbf{R},\mathbf{R}') = \frac{U_0}{\sqrt{\left(\frac{4\pi\epsilon_0}{e^2}U_0\left|\mathbf{R}-\mathbf{R}'\right|\right)^2+1}}. \tag{3.23}$$

where U_0 the on-site Coulomb potential for two π electrons at the same site $\mathbf{R}=\mathbf{R}'$, which is defined by

$$U_0 = \int d\mathbf{r}d\mathbf{r}'\varphi_\pi^2(\mathbf{r})\varphi_\pi^2(\mathbf{r}')\frac{e^2}{\mathbf{r}-\mathbf{r}'} = 11.3\ \mathrm{eV} \tag{3.24}$$

The lower energy level of the exciton in SWNTs is well-described by this Ohno potential while for higher exciton state we need a spectral consideration [55]. Here since we consider only the lowest exciton states, the Ohno potential model is sufficient. The corresponding direct and exchange terms from Eqs. (3.13) and (3.14) are now expressed by

$$\begin{aligned} K^d &= \frac{1}{2}\left\{K\left((\mathbf{k}+\mathbf{q})_{\mathrm{c}},(\mathbf{k}'-\mathbf{q})_{\mathrm{c}},\mathbf{k}_{\mathrm{c}},\mathbf{k}'_{\mathrm{v}}\right)+K\left((\mathbf{k}'-\mathbf{q})_{\mathrm{c}},(\mathbf{k}+\mathbf{q})_{\mathrm{c}},\mathbf{k}'_{\mathrm{v}},\mathbf{k}_{\mathrm{c}}\right)\right\} \\ &= \sum_{ss'=\mathrm{A,B}} C_s^{\mathrm{c}*}(\mathbf{k}+\mathbf{q})C_{s'}^{\mathrm{c}*}(\mathbf{k}'-\mathbf{q})C_s^{\mathrm{c}}(\mathbf{k})C_{s'}^{\mathrm{v}}(\mathbf{k}')\Re\left[v_{ss'}(\mathbf{q})\right], \end{aligned} \tag{3.25}$$

$$\begin{aligned} K^x &= \frac{1}{2}\left\{K\left((\mathbf{k}+\mathbf{q})_{\mathrm{c}},(\mathbf{k}'-\mathbf{q})_{\mathrm{c}},\mathbf{k}'_{\mathrm{v}},\mathbf{k}_{\mathrm{c}}\right)+K\left((\mathbf{k}'-\mathbf{q})_{\mathrm{c}},(\mathbf{k}+\mathbf{q})_{\mathrm{c}},\mathbf{k}_{\mathrm{c}},\mathbf{k}'_{\mathrm{v}}\right)\right\} \\ &= \sum_{ss'=\mathrm{A,B}} C_s^{\mathrm{c}*}(\mathbf{k}+\mathbf{q})C_{s'}^{\mathrm{c}*}(\mathbf{k}'-\mathbf{q})C_{s'}^{\mathrm{c}}(\mathbf{k})C_s^{\mathrm{v}}(\mathbf{k}')\Re\left[v_{ss'}\left(\mathbf{k}'-\mathbf{k}-\mathbf{q}\right)\right], \end{aligned} \tag{3.26}$$

where $\Re$ means taking the real part of a complex variable. Inserting Eqs. (3.17) and (3.22)

to Eqs. (3.25) and (3.26), at $\mathbf{q}=0$, the direct interaction term becomes

$$K^{\mathrm{d}}(\mathbf{k}+\mathbf{K},\mathbf{k}'+\mathbf{K})=\frac{1}{4}\left(\tilde{v}_{\mathrm{AA}}\left(0\right)-\tilde{v}_{\mathrm{A}B}\left(0\right)+\tilde{v}_{\mathrm{BA}}\left(0\right)-\tilde{v}_{\mathrm{BB}}\left(0\right)\right)=0. \tag{3.27}$$

Using the same manner we obtain

$$K^{\mathrm{d}}(\mathbf{k}+\mathbf{K},\mathbf{k}'+\mathbf{K})=K^{\mathrm{d}}(\mathbf{k}+\mathbf{K}^{'},\mathbf{k}'+\mathbf{K})=K^{\mathrm{d}}(\mathbf{k}+\mathbf{K},\mathbf{k}'+\mathbf{K}^{'})=K^{\mathrm{d}}(\mathbf{k}+\mathbf{K}^{'},\mathbf{k}'+\mathbf{K}^{'})=0, \tag{3.28}$$

and the exchange term becomes

$$K^{\mathrm{x}}(\mathbf{k}+\mathbf{K},\mathbf{k}'+\mathbf{K})=\frac{i}{2}\sin\left(\theta'-\theta\right)\tilde{v}_{\mathrm{AB}}\left(\mathbf{k}^{'}-\mathbf{k}\right), \tag{3.29}$$

$$K^{\mathrm{x}}(\mathbf{k}+\mathbf{K}^{'},\mathbf{k}'+\mathbf{K})=\frac{i}{2}\sin\left(\theta'+\theta\right)\tilde{v}_{\mathrm{AB}}\left(\mathbf{k}^{'}-\mathbf{k}\right), \tag{3.30}$$

$$K^{\mathrm{x}}(\mathbf{k}+\mathbf{K},\mathbf{k}'+\mathbf{K}^{'})=-\frac{i}{2}\sin\left(\theta'+\theta\right)\tilde{v}_{\mathrm{AB}}\left(\mathbf{k}^{'}-\mathbf{k}\right), \tag{3.31}$$

$$K^{\mathrm{x}}(\mathbf{k}+\mathbf{K}^{'},\mathbf{k}'+\mathbf{K}^{'})=-\frac{i}{2}\sin\left(\theta'-\theta\right)\tilde{v}_{\mathrm{AB}}\left(\mathbf{k}^{'}-\mathbf{k}\right), \tag{3.32}$$

where $\tilde{v}_{ij}=\Re(v_{ij})$. If we include the screening effect, we just change $v(\mathbf{q})$ to be the screened potential $w(\mathbf{q})=v(\mathbf{q})/\kappa\left(1+v\left(\mathbf{q}\right)\Pi\left(\mathbf{q}\right)\right)$. Here κ is the static dielectric constant due to electronic core states, σ band, and surrounding materials. In this calculation we use $\kappa=2.5$, and $\Pi\left(\mathbf{q}\right)$ is the RPA polarization function [42] which is given by

$$\Pi(\mathbf{q})=-2\sum_{\mathbf{k}}\left[\frac{\left|\sum_{s}C_{s}^{v*}\left(\mathbf{k}\right)C_{s}^{c}\left(\mathbf{k}+\mathbf{q}\right)\right|^{2}}{\epsilon_{\mathbf{k}+\mathbf{q}\mathrm{c}}-\epsilon_{\mathbf{k}\mathrm{v}}}+\frac{\left|\sum_{s}C_{s}^{c*}\left(\mathbf{k}\right)C_{s}^{v}\left(\mathbf{k}+\mathbf{q}\right)\right|^{2}}{\epsilon_{\mathbf{k}\mathrm{c}}-\epsilon_{\mathbf{k}+\mathbf{q}\mathrm{v}}}\right] \tag{3.33}$$

$\epsilon_{\mathbf{k}}$ is the single particle energy, and the summation over $\mathbf{k}$ is taken over all cutting lines in graphene Brillouin zone. Equations (3.27) and (3.28) proves that the direct terms K^{d} in the first-order process at $\mathbf{q}=0$ vanish, and only the exchange terms K^{x} survive. Therefore, the first-order exciton-exciton scattering give a very small contribution to the ERS spectra and then we must consider the second-order process.

Chapter 4

Electronic Raman spectra

In this chapter, we show our calculated result of the electronic Raman spectra (ERS) using Eq. (3.4). Firstly, we discuss the exciton-exciton matrix element Eq. (3.6) from extended tight binding (ETB) approximation (Sec. 4.1). We calculate the Raman intensity by considering the quantum interference of the ERS spectra with the RBM and G bands Raman spectra. In section 4.2, we compare our calculated result of laser excitation energy ($E_{\rm L}$) dependence of Raman intensity with the experimental data. By analyzing each spectra, we can fit the asymmetric line shape of G band, induced by the ERS and phonon spectra interference, with Breit-Wigner-Fano (BWF) lineshape. Finally, we discuss how the asymmetric line shapes change as a function of $E_{\rm L}$.

4.1 Exciton-exciton matrix elements

We calculate exciton-exciton matrix elements Eq. (3.6) which responsible to give the information of transition probability of the photo-excited carrier scattered by the linear band exciton. Our calculation here based on extended tight binding method (ETB).

In Fig. 4-1(a)-(c), we show the direct and the exchange Coulomb interaction processes for intra-valley and inter-valley interactions. In Fig. 4-1(d) and (e) we show the calculated direct and exchange Coulomb interaction matrix elements for a (23,14) m-SWNT, respectively. As what we expect from Eq. (3.28), both AV and EV scattering matrix elements give a zero

Fig. 4-1: fig/ch4-mxx.eps

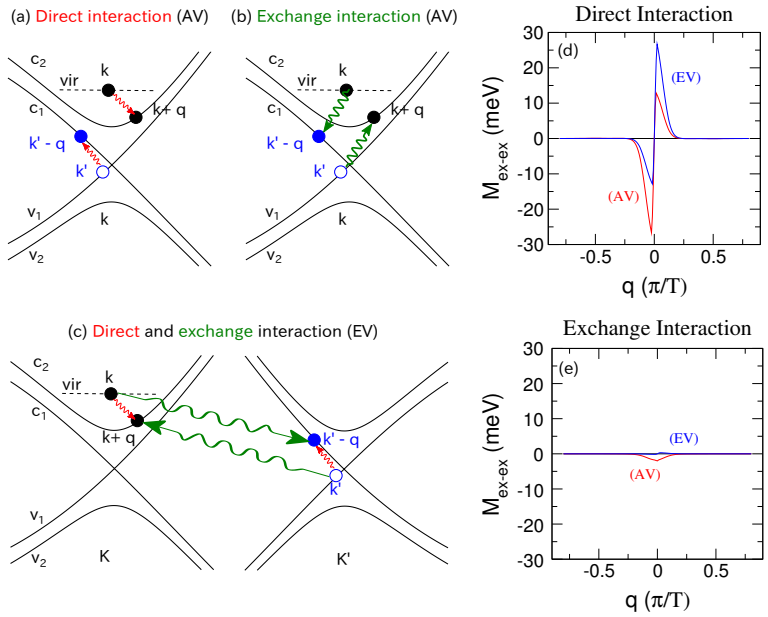

Figure 4-1: (a) The direct (AV), (b) the exchange (AV), and (c) the direct (red) and exchange (green) (EV) Coulomb interaction process. The calculated result of (d) the direct and of (e) the exchange Coulomb interaction of a (23,14) tube which has a diameter of 2.53 nm. Label AV (EV) inside each panel shows the states, in which two electrons lie in the same (different) valley. The one-dimensional (1D) wave vector $\mathbf{q}$ is projected on the 1D SWNT cutting lines and expressed in terms of the translational vector length T. We have $T = 0.46$ nm for the (23,14) tube.

value at $\mathbf{q} = 0$ for direct interaction $K^{\rm d}$ Fig. 4-1(d). At $\mathbf{q} = 0$, only the exchange interaction $K^{\rm x}$ gives a small contribution from the AV scattering (Fig. 4-1(e)). The vanishing $K^{\rm d}$ can be explained by the presence of three $C_s^{\rm c}$ and one $C_s^{\rm v}$ coefficients in Eq. (3.25). $C_{\rm B}^{j}(C_{\rm A}^{j'})$ change (does not change) the sign when we exchange c $\rightarrow$ v in j and j' (Eq. (3.17)). Thus the product of wave functions always gives an opposite sign when we exchange A $\rightarrow$ B in s or s' and thus the total summation over A and B sublattices vanishes at $\mathbf{q} = 0$ (Eq. (3.17)). As long as we incorporate three $C^{\rm c}$ and one $C^{\rm v}$ coefficients into $K^{\rm d}$, the vanishing direct Coulomb interaction at $\mathbf{q} = 0$ is a general phenomenon in graphene and SWNT systems. The results from Figs. 4-1(d) and (e) thus imply that the first-order Raman process corresponding to the AV and EV scattering at $\mathbf{q} = 0$ makes only a minor contribution to the Raman spectra. Consequently, we should consider the second-order ERS process, in which the $\mathbf{q} \neq 0$ term in $K^{\rm d}$ becomes important. It is important to note that in $K^{\rm d}$, the dominant matrix elements arises from $q \approx \pm 0.1\pi/T$ which is only 5% of the cutting line length and thus the transition is almost vertical.

4.2 $E_{\rm L}$-dependence of ERS

In Fig. 4-2(a) we show the calculated result of the $E_{\rm L}$ dependence of the Raman intensity for (23,14) m-SWNT as a function of scattered photon energy $\hbar\omega_{\rm s}$. In the present work, we only calculate the $E_{\rm L}$ dependence of the Raman intensity near $E_{22}^{\rm L} = 2.08$ eV.

We cannot reproduce exactly the relative intensity scale with the experimental data shown in Fig. 4-2 because there are many optical processes interfering with these spectra other than ERS, G, and RBM. Nevertheless, our calculated result can explain the overall behavior of the observed ERS as shown in Fig. 4-2(b). The calculated ERS feature has a very broad spectral width (FWHM$^{\rm ERS} \approx 50$ meV) with a peak intensity almost comparable to that of the RBM. Unlike the other phonon modes, whose peak positions are shifted by changing $E_{\rm L}$, the ERS peak remains at the frequency of the E_{ii} transition. At $E_{\rm L} = 2.07$ eV, the ERS spectrum starts to appear and modifies the RBM and the G band line shapes. For $E_{\rm L} = 2.07$ eV, although $E_{\rm L}$ is 10 meV below M_{22}^{L}, the energy-momentum conservation

Fig. 4-2: ch4-calex.eps

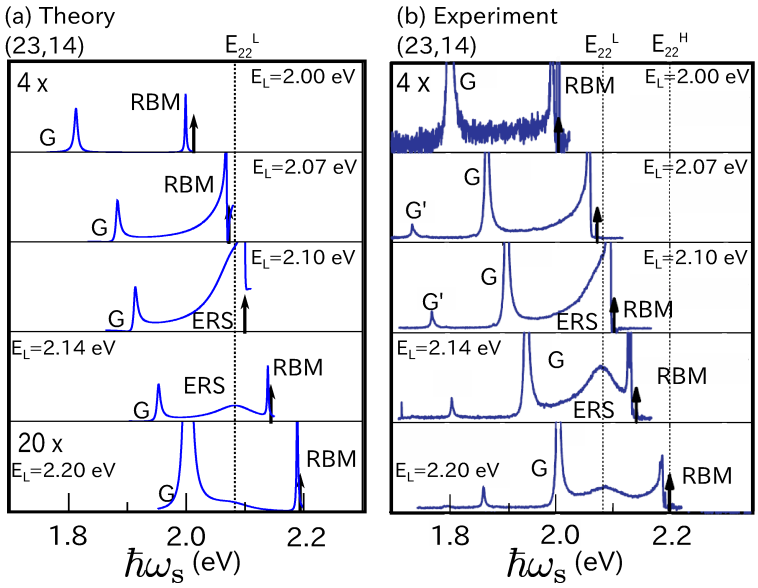

Figure 4-2: (a) Calculated result (this work) for (23,14) m-SWNT and (b) experimental results (adapted from Ref. [6]) of Raman intensity versus $\hbar\omega_s$ for a (23,14) tube where we have the calculated $E_{22}^{L} = 2.084$ eV and the experimental $E_{22}^{L} = 2.08$ eV and $E_{22}^{H} = 2.20$ eV. E_{22}^{L} and E_{22}^{H} are the splitting of transition energy in m-SWNTs due to the trigonal warping effect [34]. The laser excitation energies E_L are taken as 2.00, 2.07, 2.10, 2.14, and 2.20 eV.

during the exciton-exciton scattering may be violated by the Heisenberg uncertainty principle ($\Delta t \approx 10$ fs corresponding to $\Delta E \approx 100$ meV).

Each Raman intensity calculated from Eq. (3.4) actually gives a Lorentzian shape for all phonon modes and also for the ERS as presented in Fig. 4-3(a). However, the broad feature of the ERS overlaps with the phonon modes and thus the quantum interference between ERS and G (or RBM) gives rise to the asymmetric line shape, peak shifting, and the intensity enhancement of the G band, which can be seen as the blue solid line in the inset of Fig. 4-3 (a). We find that the asymmetric line shape of the G band after subtracting the ERS contribution clearly shows the BWF line shape, fitted by

$$I(\omega) = I_0 \frac{\left[1 + (\omega - \omega_0)/q_{\mathrm{BWF}}\Gamma\right]^2}{1 + \left[(\omega - \omega_0)/\Gamma\right]^2}, \tag{4.1}$$

where $1/q_{\mathrm{BWF}}$, Γ, and ω_0 are respectively, asymmetric factor, spectral width, and central frequency parameters to be determined (see Fig. 4-3 (b) and (c)). According to Fano [3],

Fig. 4-3: fig/ch4-ersbwf.eps

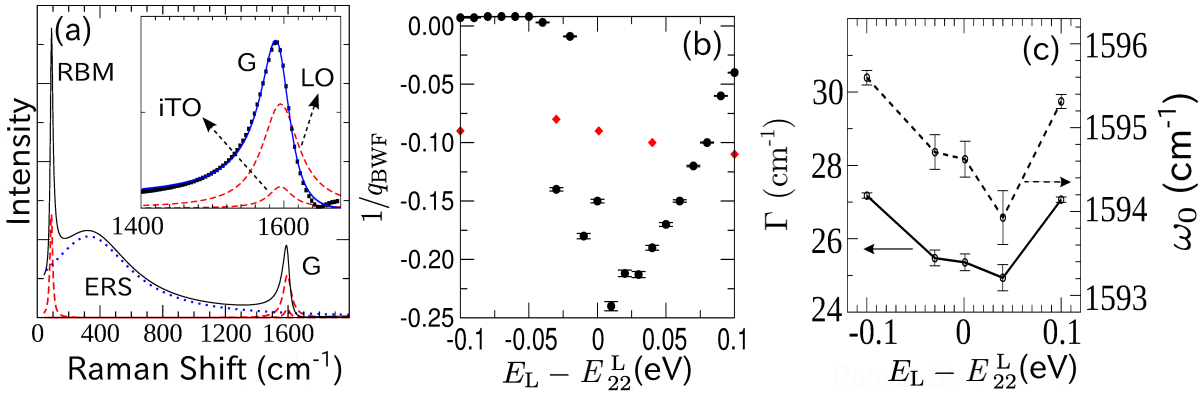

Figure 4-3: (a) Calculated Raman spectra for a (23,14) SWNT with $E_{\rm L} = 2.14$ eV. The total intensity shown is represented by the solid line. The dashed lines show contributions from the RBM and G modes, while the dotted blue line is the contribution from the ERS. Each line shape for the RBM, the G modes, and the ERS are Lorentzian. Inset shows the G band spectra after subtracted by the ERS spectrum. Filled squares are calculated results and the solid line shows the BWF fitting (Eq. (4.1)). (b) Asymmetric factor ($1/q_{\rm BWF}$) as a function of resonance condition($E_{\rm L} - E_{22}^{L}$). The black circles are calculated result and the red diamonds show experimental result [6]. (c) spectral width and peak position of the G band as a function of resonance condition ($E_{\rm L} - E_{22}^{L}$) for the (23,14) tube. The solid and dashed arrows are given as a guide for the corresponding axes.

$1/q_{\rm BWF}$ is proportional to the coupling constant between the continuum spectrum and the discrete spectrum. In our case, $1/q_{\rm BWF}$, Γ and ω_0 as a function of $E_{\rm L} - E_{22}^{L}$ give "V" shapes, with the minimum peak $\sim$ 40 meV above the resonance as depicted in Fig. 4-3(b) and (c). $1/q_{\rm BWF}$ reaches a maximum value because the intensity and the peak position of the ERS allows it to have a very strong overlap with the G band at that point. This coupling also induces the narrowing and the shifting of the G band peak closer to the ERS peak position. The calculated $1/q_{\rm BWF}$ values are in the same order with the experimental result, yet the trend does not conform. The experimental data give relative constant values even when laser excitation energy goes further away from resonance condition. This difference might arises due to different fitting of the ERS spectra which are substracted to the G band spectra.

The RBM spectral lineshapes show the similar BWF asymmetry due to RBM-ERS interference (Fig. 4.2(a) and (b)). At $E_{\rm L}$ below $E_{22}^{\rm L}$, no ERS spectra appear and thus RBM spectra give the Lorentzian lineshapes (the black lines of Fig. 4.2(a)). Around 40 meV below $E_{22}^{\rm L}$, the ERS spectra start to appear and modify the RBM and show the BWF lineshapes (the red lines of Fig. 4.2(a)). The exciton excitation below $E_{22}^{\rm L}$ is allowed by the uncertainty

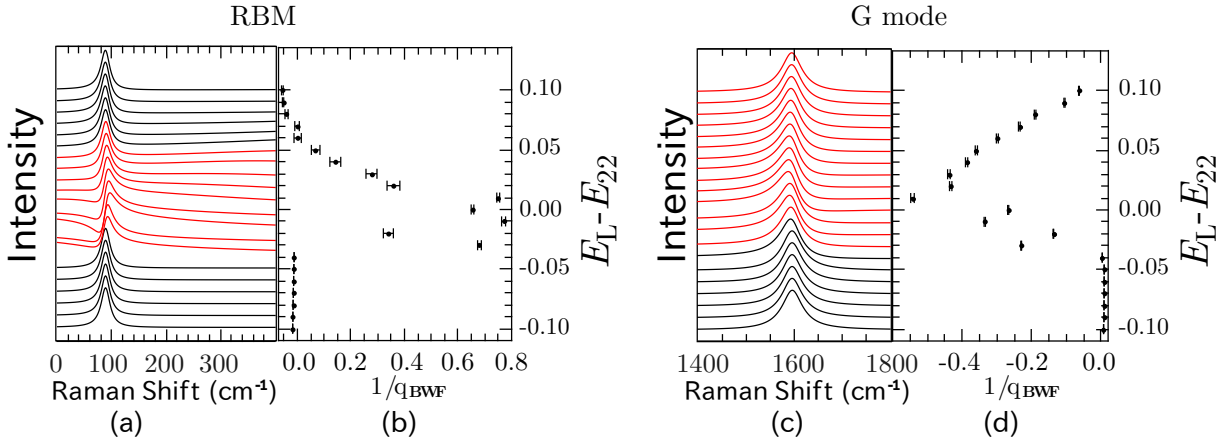

Figure 4-4: (a), (c) Cascading plot of $E_{\rm L}$ dependence of the RBM and the G mode Raman intensity (no subtraction with the ERS) as a function of Raman shift, respectively. (b), (d) The BWF asymmetric factor $1/q_{\rm BWF}$ of the RBM and the G mode as a function of resonance condition $E_{\rm L} - E_{22}^{\rm L}$, respectively with the error bars shown. $E_{\rm L}$ varies from 2.00 eV to 2.20 eV with stepsize $\Delta E_{\rm L} = 0.01$ eV. In this case $E_{22}^{\rm L} = 2.10$ eV. Black lines of the spectra show the Lorentzian lineshapes ($1/q_{\rm BWF} \approx 0$) and the read lines show the BWF lineshapes ($1/q_{\rm BWF} \neq 0$).

principle due to the finite lifetime of the exciton-exciton interaction ($\Delta t \approx 10$ fs corresponding to $\Delta E \approx 100$ meV).

In comparison to the G band asymmetry (Fig. 4.2(c), (d)), the RBM $1/q_{\rm BWF}$ gives the positive sign and the maximum value of $|1/q_{\rm BWF}|$, which appears near resonance $E_{\rm L} \approx E_{22}^{\rm L}$, is larger by difference 0.2. The large $1/q_{\rm BWF}$ in the RBM spectrum arise because at resonant condition, the ERS and the RBM are greatly enhanced and their peak positions lie very close to each other (Fig. 4-2 at $E_{\rm L} = 2.1$ eV) and thus give the strong interference effect. This RBM asymmetric lineshape in m-SWNTs has never been discussed before in any literature.

In order to explain the sign difference of $1/q_{\rm BWF}$ in the RBM and G mode spectral lineshapes, we recall the Raman intensity formula Eq. (3.4). For simplicity, we consider the ERS-RBM and ERS-G interference independently, so then we can write the intensity formula as:

$$I_\nu = |A_{\rm ERS} + A_\nu|^2 , \qquad \nu = {\rm G, RBM}. \tag{4.2}$$

From Eqs. (3.1) and (3.3), we know that Raman scattering amplitudes are generally complex. Since we are interested only in amplitude as a function of Raman shift ($\hbar\omega_{\rm s}$), we can generally

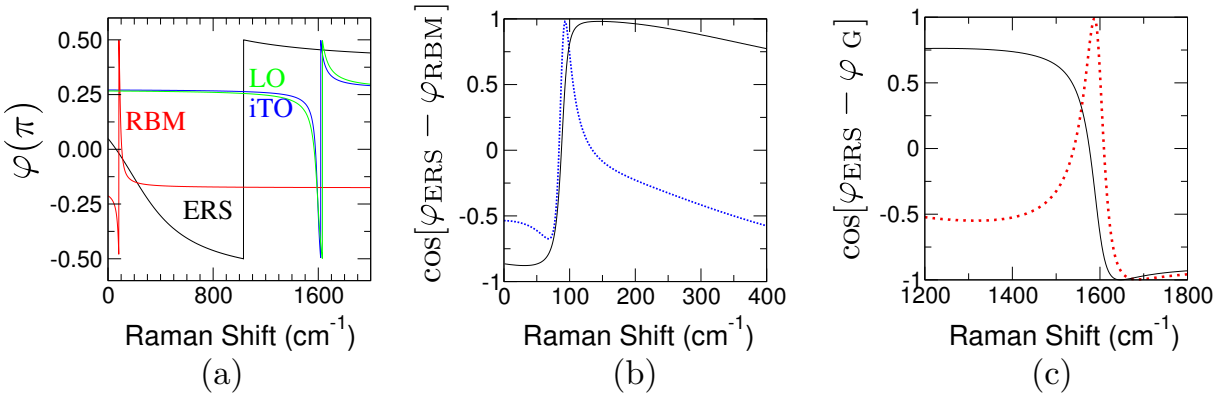

Figure 4-5: (a) Raman phase of the RBM, ERS, and G (LO and iTO) mode calculated from Eqs. (4.5), (3.1), and (3.3) at $E_{\rm L} = E_{22}^{\rm L} = 2.1$ eV. (b) and (c) Cosine of phase difference $\varphi_{\rm ERS} - \varphi_{\rm RBM}$ and $\varphi_{\rm ERS} - \varphi_{\rm G}$, respectively. Dotted line in (b) and (c) shows the RBM and G mode total intensity form Eq. (3.4), respectively. Asymmetric factor $1/q_{\rm BWF} = 0.65$ for RBM and $1/q_{\rm BWF} = -0.27$ for G mode.

write Eqs. (3.1) and (3.3) as

$$A_\nu(\Omega_\nu) = \frac{\alpha_\nu + i\beta_\nu}{\Omega_\nu - i\Gamma_\nu}, \qquad \nu = \text{RBM},\ \text{ERS},\ \text{G} \tag{4.3}$$

where $\Omega_\nu = E_{\rm L} - \hbar\omega_\nu - \hbar\omega_{\rm s}$ for $\nu = $ RBM, G (Eq. (3.1)) and for ERS $\Omega_{\rm ERS} = E_{\rm L} - \hbar\omega_1 - \hbar\omega_2 - \hbar\omega_{\rm s}$ (Eq. (3.3)). α_ν and β_ν are defined by the real and imaginary parts of amplitudes terms otherwise contain $\hbar\omega_{\rm s}$. Now we can can write Eq. 4.2 as

$$I_\nu = |A_{\rm ERS}|^2 + |A_\nu|^2 + 2|A_{\rm ERS}||A_\nu|\cos(\varphi_{\rm ERS} - \varphi_\nu), \qquad \nu = \text{G}, \text{RBM}, \tag{4.4}$$

where φ_ν is the Raman phase for ν (= ERS, G, RBM) Raman spectra given by

$$\varphi_\nu = \arctan\left(\frac{\text{Im}(A_\nu)}{\text{Re}(A_\nu)}\right) = \arctan\left(\frac{\beta_\nu\Omega_\nu + \Gamma_\nu\alpha_\nu}{\alpha_\nu\Omega_\nu - \Gamma_\nu\beta_\nu}\right). \tag{4.5}$$

Eq. (4.5) shows that Raman phase shifts at $\Omega_\nu = \dfrac{\Gamma_\nu\beta_\nu}{\alpha_\nu}$.

In Fig. 4-5(a), we show the calculated Raman phase of the RBM, ERS, and G (LO and iTO) mode calculated from Eqs. (4.5), (3.1), and (3.3) at $E_{\rm L} = E_{22}^{\rm L} = 2.1$ eV. Phase shift from $-\pi/2 \to \pi/2$ appears in each Raman spectra as described by Eq. (4.5). In case of RBM and G, Γ contribution in phase shift is negligible so that phase shift appears very close to

resonance $\hbar\omega_{\rm s} = E_{\rm L} - \hbar\omega_{\nu}$. Because of this phase shift at the resonance, the interference term of Raman intensity (Eq. (4.4) drastically change their sign depicted in Figs. 4-5(b) and (c). The sign change from negative (positive) to positive (negative) correspond to positive (negative) $1/q_{\rm BWF}$ because of the ERS phase shift position is at right (left) of the RBM (G mode).

Chapter 5

Conclusion

We have formulated a theoretical calculation for the electronic Raman scattering (ERS) by considering the exciton-exciton interaction. We showed that in the direct Coulomb interaction the zero momentum transfer process $\mathbf{q} = 0$ vanishes due to the symmetry of the SWNT sublattices. We found that this fact is a general phenomenon occurring not only in carbon sp^2 systems but also in any material which has the same symmetry. Next, by considering a $\mathbf{q} \neq 0$ second-order process, we can consistently reproduce the ERS spectra from experiment as a function of E_{L}. This ERS spectrum is coupled with the G band and the interference with the ERS spectrum shows the Breit-Wigner-Fano (BWF) line shape of the G band. The asymmetry, narrowing, and shifting of the G band induced by the interference with the ERS are all sensitive to the peak intensity ratio and the peak distance between the ERS and the G band. The calculated BWF asymmetric factor is consistent with the experimental result. We also predict that the RBM also exhibit the similar asymmetry due to quantum interference effect with the ERS. Opposite from the G band asymmetry which shows negative sign of asymmetric factor $1/q_{\mathrm{BWF}}$, the RBM shows positive $1/q_{\mathrm{BWF}}$. This RBM asymmetry in m-SWNTs has never been discussed before in any literature.

Appendix A

Exciton-photon and exciton-phonon matrix elements

A.1 Exciton-photon matrix elements

We calculate the electron-photon matrix element $M_{\mathrm{el-op}}$ in the dipole approximation [52, 56, 57],

$$M_{\mathrm{el-op}} \propto \mathbf{D}(\mathbf{k}', \mathbf{k}) \cdot \mathbf{P}, \tag{A.1}$$

with $\mathbf{D}(\mathbf{k}', \mathbf{k}) = \langle \psi(\mathbf{k}') | \nabla | \psi(\mathbf{k}) \rangle$ being the dipole vector between the initial and final states, and $\mathbf{P}$ being the polarization of the incident light. In the case of parallel polarization, the dipole selection rule for $\mathbf{k}$ gives $\mathbf{k}' = \mathbf{k}$, and we can write the el-op Hamiltonian as

$$H_{\mathrm{el-op}} = \sum_{\mathbf{k}} D_{\mathbf{k}} c^{+}_{\mathbf{k}c} c_{\mathbf{k}v} (a + a^{+}), \tag{A.2}$$

where we have neglected a constant in the optical matrix element $M_{\mathrm{el-op}}$, $D_{\mathbf{k}}$ is the z component of $\mathbf{D}(\mathbf{k}, \mathbf{k})$, $c^{+}_{\mathbf{k}c}$ ($c_{\mathbf{k}v}$) is the electron creation (annihilation) operator in the conduction (valence) band, and a^{+} (a) is the photon creation (annihilation) operator.

The exciton wavefunction $|\Psi^{n}_{\mathbf{q}}\rangle$ with a center-of-mass momentum $\mathbf{q}$ can be expressed by

a linear combination of the $\mathbf{k}$ states as

$$|\Psi^n_{\mathbf{q}}\rangle = \sum_{\mathbf{k}} Z^n_{\mathbf{k}c,(\mathbf{k}-\mathbf{q})v} c^+_{\mathbf{k}c} c_{(\mathbf{k}-\mathbf{q})v} |0\rangle, \tag{A.3}$$

where $Z^n_{\mathbf{k}c,(\mathbf{k}-\mathbf{q})v}$ is the eigenvector of the n-th ($n = 1, 2, \cdots$) state of the Bethe-Salpeter equation, and $|0\rangle$ is the ground state. The summation on $\mathbf{k}$ is taken for all cutting-lines in the two-dimensional Brillouin zone (2D BZ). However, the summation on a cutting line of a k state is sufficient [42] because the range of the Ohno potential in the $k-$ space is smaller than the distance of two adjacent cutting lines $2/d_t$. Due to momentum conservation, the photon-excited exciton is an exciton with $\mathbf{q} = 0$. From Eqs. (A.2) and (A.3), we get the ex-op matrix element between an excited state $|\Psi^n_0\rangle$ and the ground state $|0\rangle$,

$$M_{\mathrm{ex-op}} = \langle \Psi^n_0 | H_{\mathrm{el-op}} | 0 \rangle = \sum_{\mathbf{k}} D_{\mathbf{k}} Z^{n*}_{\mathbf{k}c,\mathbf{k}v}. \tag{A.4}$$

Because of the existence of two inequivalent valleys (K and K′), among the four symmetries of C_2 rotation along the axis at the center of a C-C bond, only the A_2 exciton is bright, while other A_1, E and E^* excitons are dark (Sec. 2.2.2). A_1 and A_2 excitons are symmetric and antisymmetric under a C_2 rotation, respectively. The wavefunction for an A_1 (A_2) exciton with $\mathbf{q} = 0$ is given by

$$|\Psi^n_0(A_{1,2})\rangle = \frac{1}{\sqrt{2}} \sum_{\mathbf{k}} Z^n_{\mathbf{k}c,\mathbf{k}v} (c^+_{\mathbf{k}c} c_{\mathbf{k}v} \mp c^+_{-\mathbf{k}c} c_{-\mathbf{k}v}) |0\rangle, \tag{A.5}$$

where $\mathbf{k}$ and $-\mathbf{k}$ are around the K and K$'$ points, respectively, and $-$ $(+)$ in $\mp$ is for an A_1 (A_2) exciton.

When we use the relation $D_{\mathbf{k}} = D_{-\mathbf{k}}$, the ex-op matrix elements for the A_1 and A_2 excitons are given

$$\begin{aligned} M_{\mathrm{ex-op}}(A^n_1) &= 0, \\ M_{\mathrm{ex-op}}(A^n_2) &= \sqrt{2} \sum_{\mathbf{k}} D_{\mathbf{k}} Z^{n*}_{\mathbf{k}c,\mathbf{k}v}. \end{aligned} \tag{A.6}$$

Equation (A.6) directly indicates that A_1 excitons are dark and only A_2 excitons are bright, which is consistent with the predictions by group theory[58].

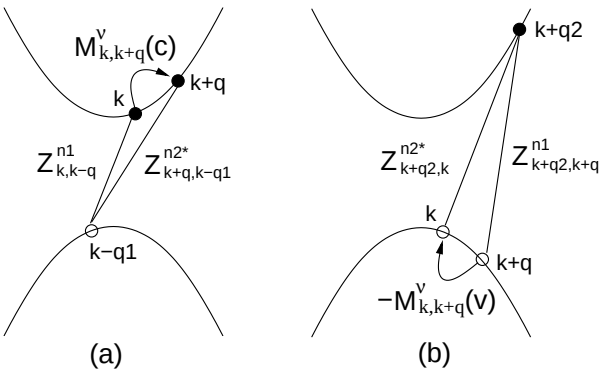

Figure A-1: (a) electron and (b) hole scattering processes in the ex-ph matrix element for the first and second terms of Eq. (A.8). The matrix element for (a) and (b) is determined by the electron and hole matrix elements weighted by the wavefunction coefficients from the initial and final states [50].

A.2 Exciton-phonon matrix elements

The Hamiltonian for the electron-phonon coupling for a phonon mode $(\mathbf{q}, \nu)$ has the form

$$H_{\mathrm{el-ph}} = \sum_{\mathbf{k}\mathbf{q}\nu} \left[M^{\nu}_{\mathbf{k},\mathbf{k}+\mathbf{q}}(c) c^{+}_{(\mathbf{k}+\mathbf{q})c} c_{\mathbf{k}c} - M^{\nu}_{\mathbf{k},\mathbf{k}+\mathbf{q}}(v) c^{+}_{(\mathbf{k}+\mathbf{q})v} c_{\mathbf{k}v} \right] (b_{\mathbf{q}\nu} + b^{+}_{\mathbf{q}\nu}), \tag{A.7}$$

where $M(c)$ $(M(v))$ is the el-ph matrix element for the conduction (valence) band, and $b^{+}_{\mathbf{q}\nu}$ $(b_{\mathbf{q}\nu})$ is a phonon creation (annihilation) operator for the νth phonon mode at $\mathbf{q}$ [59].

From Eq. (A.7), we obtain the ex-ph matrix element between the initial state $|\Psi^{n1}_{\mathbf{q}1}\rangle$ and a final state $|\Psi^{n2}_{\mathbf{q}2}\rangle$,

$$\begin{aligned} M_{\mathrm{ex-ph}} &= \langle \Psi^{n2}_{\mathbf{q}2} | H_{\mathrm{el-ph}} | \Psi^{n1}_{\mathbf{q}1} \rangle \\ &= \sum_{\mathbf{k}} \left[M^{\nu}_{\mathbf{k},\mathbf{k}+\mathbf{q}}(c) Z^{n2*}_{\mathbf{k}+\mathbf{q},\mathbf{k}-\mathbf{q}1} Z^{n1}_{\mathbf{k},\mathbf{k}-\mathbf{q}1} - M^{\nu}_{\mathbf{k},\mathbf{k}+\mathbf{q}}(v) Z^{n2*}_{\mathbf{k}+\mathbf{q}2,\mathbf{k}} Z^{n1}_{\mathbf{k}+\mathbf{q}2,\mathbf{k}+\mathbf{q}} \right], \end{aligned} \tag{A.8}$$

with $\mathbf{q} = \mathbf{q}2 - \mathbf{q}1$ giving the momentum conservation. The energy conservation for ex-ph scattering is given by $E^{n2}_{\mathbf{q}2} - E^{n1}_{\mathbf{q}1} = E_{\mathrm{ph}}$ for phonon absorption, and $E^{n1}_{\mathbf{q}1} - E^{n2}_{\mathbf{q}2} = E_{\mathrm{ph}}$ for phonon emission $(b_{\mathbf{q},\nu})$. In the following, we will consider only the Stokes (phonon emission) process and we will not explicitly write the phonon number in $|\Psi^{n}_{\mathbf{q}}\rangle$.

Figure A-1 schematically illustrates the electron and hole scattering processes in the ex-ph matrix element, which corresponds to the first and second terms in Eq. (A.8), respectively.

Figure A-1(a) shows that the ex-ph matrix element from the electron scattering process is the el-ph matrix element $M^{\nu}_{\mathbf{k},\mathbf{k}+\mathbf{q}}(c)$ weighted by the wavefunction coefficient $Z^{n2*}_{\mathbf{k}+\mathbf{q},\mathbf{k}-\mathbf{q}1}$ for an electron-hole (e-h) pair with the electron at $\mathbf{k}+\mathbf{q}$ in the final state $|\Psi^{n2}_{\mathbf{q}2}\rangle$ and the coefficient $Z^{n1}_{\mathbf{k},\mathbf{k}-\mathbf{q}1}$ for an e-h pair with the electron at $\mathbf{k}$ in the initial state $|\Psi^{n1}_{\mathbf{q}1}\rangle$. Figure A-1(b) shows that the ex-ph matrix element from the hole scattering process is the hole-phonon matrix element $-M^{\nu}_{\mathbf{k},\mathbf{k}+\mathbf{q}}(v)$ weighted by the wavefunction coefficient $Z^{n2*}_{\mathbf{k}+\mathbf{q}2,\mathbf{k}}$ for an e-h pair with the hole at $\mathbf{k}$ in the final state $|\Psi^{n2}_{\mathbf{q}2}\rangle$ and the coefficient $Z^{n1}_{\mathbf{k}+\mathbf{q}2,\mathbf{k}+\mathbf{q}}$ for an e-h pair with the hole at $\mathbf{k}+\mathbf{q}$ in the initial state $|\Psi^{n1}_{\mathbf{q}1}\rangle$.

Appendix B

Virtual state approximation

When an electron in a ground state absorbs a photon with energy E_{L}, the exciton generated will occupy a virtual state in which the photon energy may not be resonant with any exciton energy states. We can then define the virtual state as a linear combination of the exciton states:

$$|\Psi^{\mathrm{vir}}\rangle = \sum_{n} A_n |n\rangle \tag{B.1}$$

where $|n\rangle = \sum_{\mathbf{k}} Z^{n}_{\mathbf{kc},\mathbf{kv}} c^{\dagger \mathrm{c}}_{\mathbf{k}} c^{\mathrm{v}}_{\mathbf{k}} |g\rangle$ is the n-th exciton state and A_n is the coefficient of transition from the ground state $|g\rangle$ to $|n\rangle$ which is determined from time-dependent perturbation theory (TDPT). From the TDPT calculation we obtain

$$A_n(E_{\mathrm{L}}, t) = \sqrt{N} \mathcal{M}^{n,g}_{\mathrm{ex-op}} \frac{\sin(E_{\mathrm{L}} - E_n)t/2\hbar}{E_{\mathrm{L}} - E_n}, \tag{B.2}$$

where N is the normalization constant to guarantee $\sum_n |A_n|^2 = 1$. We eliminate the time dependency by taking the root mean square over time with $\lim \tau \to \infty$. We then obtain the average transition probability:

$$\langle A^2_n(E_{\mathrm{L}}) \rangle_\tau = N \left(\frac{\mathcal{M}^{n,g}_{\mathrm{ex-op}}}{E_{\mathrm{L}} - E_n - i\gamma} \right)^2 . \tag{B.3}$$

where we have included a phenomenological quasi particle life time $\gamma \approx 60$ meV. From Eq. (B.3), we can say that the transition probability in state n is determined by the exciton-photon matrix elements and by the resonance condition of that energy state to E_{L}.

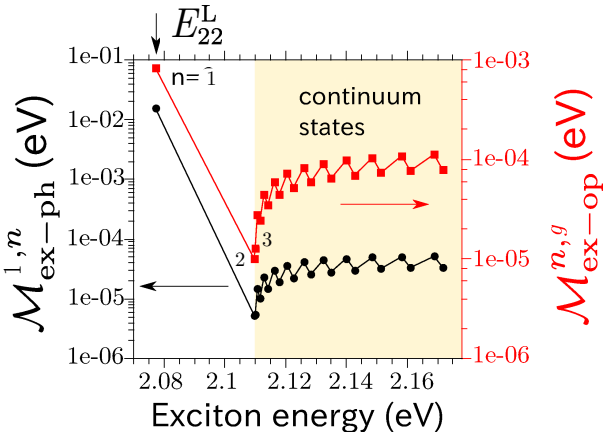

Figure B-1: LO exciton-phonon matrix element from the n-th state to the lowest exciton state $\mathcal{M}_{\mathrm{ex-ph}}^{1,n}$ and exciton-photon matrix element $\mathcal{M}_{\mathrm{ex-op}}^{n,i}$ from the initial state to the n-th exciton state [50].

In Eq. (5) we approximate the virtual state as the lowest exciton state. We can justify the approximation based on a calculation of Raman intensity resulting from each exciton state. In order to obtain the intensity contribution from each state, we use Eqs. (B.1) and (B.3) to Eq. (3.1) for the LO mode and set $\hbar\omega_s = M_{22}^{\mathrm{L}}$, assuming that in $\mathcal{M}_{\mathrm{ex-ph}}$ a photo-excited exciton from the n-th state emits a phonon and always relaxes to the lowest exciton state $n = 1$. Figure B-1 shows that $\mathcal{M}_{\mathrm{ex-ph}}^{1,n=1}$ ($\mathcal{M}_{\mathrm{ex-op}}^{n=1,i}$) is typically three orders (one order) of magnitude larger than that in the continuum states. Therefore, the relative Raman intensity from the lowest exciton state I^0 is almost ten orders larger than that in the continuum states. Based on this result, we dismiss the contributions of the continuum exciton states to the virtual state.

Fig. B-1: fig/ap-sfig2.eps

Appendix: calculation program

The main program to calculate the electronic Raman spectra for a single chirality m-SWNT based on the work by Jiang *et al.* [42, 50] and Sato *et al.* [36]. All the necessary programs can be found under the following directory in `FLEX` workstation:

`~hasdeo/for/mxxders/`

Hereafter, this directory will simply be referred to as `ROOT/` directory. More detail explanations about how to use the programs are given in the `00README` file in each subdirectory of `ROOT`.

Electronic Raman spectra for a single chirality

Main program: `ROOT/ers-onetube.f90`

Inputs:

1. `subband INTEGER` the ii value for E_{ii} transition energy. In metallic SWNT, we define ii value as following
   - `subband = 0` for linear band
   - `subband = 1` for E_{11}^{L}
   - `subband = 2` for E_{11}^{H}
   - `subband = 3` for E_{22}^{L}
   - `subband = 4` for E_{22}^{H}
   - etc.
2. `n, m INTEGER` the nanotube chiral index.

3. `phmode INTEGER` phonon mode. We specify RBM, iTO, or LO by using the following value
   - `phmode = 3` for RBM
   - `phmode = 5` for LO
   - `phmode = 6` for iLO
4. `elmin, elmax REAL(8)` minimum and maximum laser excitation energy (eV)

Exciton energies and exciton wave functions

Subroutine: `ROOT/exh.f90` Construct exciton hamiltonian and calculate its eigenvalues and eigenvectors

Outputs: 1. `exval REAL(8), dimension (bound)` exciton energy. `exval(1)`$= E_{ii}$ by definition. `INTEGER, parameter:: bound= 2000`

2. `exvec COMPLEX (8), dimension (bound,bound)` exciton eigenvector solved from the Bethe-Salpeter equation. `exvec (k,l)` will give the exciton eigenvector for `k` relative-motion momentum at `l` state.

Exciton-photon matrix element

Subroutine: `ROOT/exopmx.f90` Calculate the exciton photon matrix elements.

Outputs: 1. `mexopd COMPLEX(8)` exciton-photon matrix element with unit 1/nm.

2. `mexopm COMPLEX(8)` exciton-photon matrix element with unit eV.

Exciton-phonon matrix element

Subroutine: `ROOT/exphmx.f90` Calculate the exciton phonon matrix elements.

Outputs: 1. `dmx COMPLEX(8)` exciton-phonon matrix element with unit eV/nm.

2. `mmx COMPLEX(8)` exciton-phonon matrix element with unit eV.

Exciton-exciton matrix element

Subroutine: `ROOT/iniga-diaex.f90` Calculate the exciton-exciton matrix elements.

Outputs: 1. `mxx COMPLEX(8) dimension (2,4,2,-100:100)` The exciton-exciton matrix elements. We define exciton-exciton matrix element as `mxx (spin,valley,k,q)`, where

- `s= 1` for singlet spin
- `s=2` for triplet spin.
- `valley= 1` intravalley interaction (A) intravalley scattering (a)
- `valley= 2` intravalley interaction (A) intervalley scattering (e)
- `valley= 3` intervalley interaction (E) intravalley scattering (a)
- `valley= 4` intervalley interaction (E) intervalley scattering (e)
- `k=1` photo-excited exciton at K point
- `k=2` photo-excited exciton at K′ point

Publication list

Papers

1. **E. H. Hasdeo**, A. R. T. Nugraha, K. Sato, R. Saito, M. S. Dresselhaus, Origin of electronic Raman scattering and the Fano resonance in metallic carbon nanotubes, arXiv:1301.7585 (2013).

2. A. R. T. Nugraha, E. Rosenthal, **E. H. Hasdeo**, G. D. Sanders C. J. Stanton, M. S. Dresselhaus, R. Saito, Excitonic effects on coherent phonon dynamics in single wall carbon nanotubes, arXiv:1305.1424 (2013).

Conferences

Oral presentations

1. **Eddwi Hesky Hasdeo**, Ahmad Ridwan Tresna Nugraha, Kentaro Sato, Riichiro Saito: Theory of electronic Raman scattering in metallic single wall carbon nanotubes. Presented in ATI 2012 Nano-Carbon Meeting and Zao12 Meeting (22-23 July 2012), Yamagata-Zao, Japan.

Poster Presentations

1. Riichiro Saito, **Eddwi Hesky Hasdeo**, Ahmad Ridwan Tresna Nugraha, Kentaro Sato, Mildred Dresselhaus: Electronic Raman scattering and origin of the Fano resonance in metallic carbon nanotubes. Presented in NT13: The Fourteenth International

Conference on the Science and Application of Nanotubes (24-28 June 2013), Aalto University, Finland.

2. **Eddwi Hesky Hasdeo**, Ahmad Ridwan Tresna Nugraha, Kentaro Sato, Riichiro Saito: Electronic Raman scattering and origin of the Fano resonance in metallic carbon nanotubes. Presented in the 44rd Fullerene-Nanotubes-Graphene General Symposium (11-13 March 2013), Tokyo University, Japan.

3. **Eddwi Hesky Hasdeo**, Ahmad Ridwan Tresna Nugraha, Kentaro Sato, Riichiro Saito: Theory of electronic Raman scattering in metallic single wall carbon nanotubes. Presented in the 2012 A3 Symposium of Emerging Materials (29-31 October 2012), Tohoku University, Japan.

4. **Eddwi Hesky Hasdeo**, Ahmad Ridwan Tresna Nugraha, Kentaro Sato, Riichiro Saito: Theory of electronic Raman scattering in metallic single wall carbon nanotubes. Presented in the 43rd Fullerene-Nanotubes-Graphene General Symposium (5-7 September 2012), Tohoku University, Japan.

Bibliography

[1] V. V. Deshpande, B. Chandra, R. Caldwell, D. S. Novikov, J. Hone, and M. Bockrath, Science **323**(5910), 106–110 (2009).

[2] S. D. M. Brown, A. Jorio, P. Corio, M. S. Dresselhaus, G. Dresselhaus, R. Saito, and K. Kneipp, Phys. Rev. B **63**, 155414 (2001).

[3] U. Fano, Phys. Rev. **124**, 1866–1878 (1961).

[4] L. Alvarez, A. Righi, T. Guillard, S Rols, E. Anglaret, D. Laplaze, and J. Sauvajol, Chemical Physics Letters **316**, 186 – 190 (2000).

[5] H. Kataura, Y. Kumazawa, Y. Maniwa, I. Umezu, S. Suzuki, Y. Ohtsuka, and Y. Achiba, Synth. Met. **103**, 2555 (1999).

[6] H. Farhat, S. Berciaud, M. Kalbac, R. Saito, T. F. Heinz, M. S. Dresselhaus, and J. Kong, Phys. Rev. Lett. **107**, 157401 (2011).

[7] M.S. Dresselhaus, G. Dresselhaus, R. Saito, and A. Jorio, Physics Reports **409**(2), 47 – 99 (2005).

[8] A. Jorio, M.A. Pimenta, A.G. Souza Filho, R. Saito, G. Dresselhaus, and M.S. Dresselhaus, New Journal of Physics **5** (2003).

[9] J. S. Park. *Double Resonance Raman Spectroscopy of Single Wall Carbon Nanotubes and Graphene*. PhD thesis, Tohoku University, 2008.

[10] K. K. Kim, J. S. Park, S. J. Kim, H. Z. Geng, K. H. An, C. Yang, K. Sato, R. Saito, and Y. H. Lee, Phys. Rev. B **76**, 205426 (2007).

[11] R. Saito, M. Fujita, G. Dresselhaus, and M. S. Dresselhaus, Appl. Phys. Lett. **60**, 2204 (1992).

[12] A. Jorio, A. G. Souza-Filho, G. Dresselhaus, M. S. Dresselhaus, A. K. Swan, M. S. Ünlü, B. B. Goldberg, M. A. Pimenta, J. H. Hafner, C. M. Lieber, and R. Saito, Phys. Rev. B **65**, 155412 (March 2002).

[13] A. Jorio, A. G. Souza Filho, G. Dresselhaus, M. S. Dresselhaus, R. Saito, J. H. Hafner, C. M. Lieber, F. M. Matinaga, M. S. S. Dantas, and M. A. Pimenta, Phys. Rev. B **63**, 245416 (June 2001).

[14] P. T. Araujo, P. B. C. Pesce, M. S. Dresselhaus, K. Sato, R. Saito, and A. Jorio, Physica E **42**, 1251 – 1261 (2010).

[15] H. Farhat, H. Son, Ge. G Samsonidze, S. Reich, M. S. Dresselhaus, and J. Kong, Phys. Rev. Lett. **99**, 145506 (2007).

[16] K. Sasaki, R. Saito, G. Dresselhaus, M. S. Dresselhaus, H. Farhat, and J. Kong, Phys. Rev. B **78**, 235405 (2008).

[17] J. S. Park, K. Sasaki, R. Saito, W. Izumida, M. Kalbac, H. Farhat, G. Dresselhaus, and M. S. Dresselhaus, Phys. Rev. B **80**, 081402 (2009).

[18] P. T. Araujo, D. L. Mafra, K. Sato, R. Saito, J. Kong, and M. S. Dresselhaus, Phys. Rev. Lett. **109**, 046801 (2012).

[19] D. Yoon, D. Jeong, H. Lee, R. Saito, Y. Son, H. Lee, and H. Cheong, Carbon (0), – (2013). to be published.

[20] P. C. Eklund and K. R. Subbaswamy, Phys. Rev. B **20**, 5157–5161 (1979).

[21] Rodney Loudon, Am. J. Phys. **27**(9), 649 (1959).

[22] Y. Z. Ma, L. Valkunas, S. M. Bachilo, and G. R. Fleming, J. Phys. Chem. B **109**, 15671–15674 (2005).

[23] Tsuneya Ando, J. Phys. Soc. Jpn. **66**, 1066 (1997).

[24] J. Maultzsch, R. Pomraenke, S. Reich, E. Chang, D. Prezzi, A. Ruini, E. Molinari, M. S. Strano, C. Thomsen, and C. Lienau, Phys. Rev. B **72**, 241402 (2005).

[25] F. Wang, D. J. Cho, B. Kessler, J. Deslippe, P. J. Schuck, S. G. Louie, A. Zettl, T. F. Heinz, and Y. R. Shen, Phys. Rev. Lett. **99**, 227401 (2007).

[26] Jack Deslippe, Catalin D. Spataru, David Prendergast, and Steven G. Louie, Nano Letters **7**(6), 1626–1630 (2007).

[27] A. R. T. Nugraha, R. Saito, K. Sato, P. T. Araujo, A. Jorio, and M. S. Dresselhaus, (2010). unpublished.

[28] V. M. Adamyan, O. A. Smyrnov, and S. V. Tishchenko, J. Phys: Conf. Series **129**, 012012 (2008).

[29] Tsuneya Ando, J. Phys. Soc. Jpn. **79**(2), 024706 (2010).

[30] P. T. Araujo and A. Jorio, Phys. Status Solidi B **245**, 2201 – 2204 (2008).

[31] Georgii Samsonidze. *Photophysics of Carbon Nanotubes*. Ph. D. thesis, Massachusetts Institute of Technology, Department of Electrical Engineering and Computer Science, October 2006.

[32] Valentin N Popov, New J. Phys. **6**, 17 (2004).

[33] G. S. Painter and D. E. Ellis, Phys. Rev. B **1**, 4747 (1970).

[34] R. Saito, G. Dresselhaus, and M. S. Dresselhaus, Phys. Rev. B **61**, 2981–2990 (2000).

[35] Ge. G. Samsonidze, R. Saito, A. Jorio, M. A. Pimenta, A. G. Souza Filho, A. Grüneis, G. Dresselhaus, and M. S. Dresselhaus, J. Nanoscience and Nanotech. **3**, 431–458 (2003).

[36] K. Sato, R. Saito, J. Jiang, G. Dresselhaus, and M. S. Dresselhaus, Phys. Rev. B **76**, 195446 (2007).

[37] S. M. Bachilo, M. S. Strano, C. Kittrell, R. H. Hauge, R. E. Smalley, and R. B. Weisman, Science **298**, 2361 (2002).

[38] R. Bruce Weisman and Sergei M. Bachilo, Nano Lett. **3**, 1235 (2002).

[39] A. Jorio, M. A. Pimenta, A. G. G. Souza Filho, Ge. G. Samsonidze, A. K. Swan, M. S. S. Ünlü, B. B. Goldberg, R. Saito, G. Dresselhaus, and M. S. Dresselhaus, Phys. Rev. Lett. **90**, 107403 (2003).

[40] D. Porezag, Th. Frauenheim, Th. Köhler, G. Seifert, and R. Kaschner, Phys. Rev. B **51**, 12947 (1995).

[41] Ge. G. Samsonidze, R. Saito, N. Kobayashi, A. Grüneis, J. Jiang, A. Jorio, S. G. Chou, G. Dresselhaus, and M. S. Dresselhaus, Appl. Phys. Lett. **85**, 5703 (2004).

[42] J. Jiang, R. Saito, Ge. G. Samsonidze, A. Jorio, S. G. Chou, G. Dresselhaus, and M. S. Dresselhaus, Phys. Rev. B **75**, 035407 (2007).

[43] E. E. Salpeter and H. A. Bethe, Phys. Rev. **84**, 1232 (1951).

[44] M. Rohlfing and S. G. Louie, Phys. Rev. B **62**, 4927 (2000).

[45] R. Saito, K. Sato, Y. Oyama, J. Jiang, Ge. G. Samsonidze, G. Dresselhaus, and M. S. Dresselhaus, Phys. Rev. B **72**, 153413 (2005).

[46] R. Saito, G. Dresselhaus, and M. S. Dresselhaus, *Physical Properties of Carbon Nanotubes* (Imperial College Press, London, 1998).

[47] C. L. Kane and E. J. Mele, Phys. Rev. Lett. **90**(20), 207401 (May 2003).

[48] K. Sato, R. Saito, A. R.T. Nugraha, and S. Maruyama, Chem. Phys. Lett. **497**, 94 – 98 (2010).

[49] M. Lazzeri, S. Piscanec, Francesco Mauri, A. C. Ferrari, and J. Robertson, Phys. Rev. B **73**, 155426 (2006).

[50] J. Jiang, R. Saito, K. Sato, J. S. Park, Ge. G. Samsonidze, A. Jorio, G. Dresselhaus, and M. S. Dresselhaus, Phys. Rev. B **75**, 035405 (2007).

[51] E. B. Barros, A. Jorio, Ge. G. Samsonidze, R. B. Capaz, A. G.Souza Filho, J. Mendez Filho, G. Dresselhaus, and M. S. Dresselhaus, Physics Reports **431**, 261–302 (2006).

[52] A. Grüneis, R. Saito, Ge. G. Samsonidze, T. Kimura, M. A. Pimenta, A. Jorio, A. G. Souza Filho, G. Dresselhaus, and M. S. Dresselhaus, Phys. Rev. B **67**, 165402 (2003).

[53] V. Perebeinos, J. Tersoff, and P. Avouris, Phys. Rev. Lett. **92**, 257402 (2004).

[54] T. Ando, J. Phys. Soc. Jp. **75**(2), 024707 (2006).

[55] R. B. Capaz, C. D. Spataru, S. Ismail-Beigi, and S. G. Louie, Phys. Rev. B **74**, 121401 (2006).

[56] J. Jiang, R. Saito, A. Grüneis, G. Dresselhaus, and M. S. Dresselhaus, Carbon **42**, 3169–3179 (2004).

[57] R. Saito, A. Grüneis, Ge. G. Samsonidze, G. Dresselhaus, M. S. Dresselhaus, A. Jorio, L. G. Cançado, M. A. Pimenta, and A. G. Souza, Appl. Phys. A **78**, 1099–1105 (2004).

[58] E. B. Barros, R. B. Capaz, A. Jorio, Ge. G. Samsonidze, A. G.Souza Filho, S. Ismail-Beigi, C. D. Spataru, S. G. Louie, G. Dresselhaus, and M. S. Dresselhaus, Phys. Rev. B Rapid **73**, 241406(R) (2006).

[59] J. Jiang, R. Saito, Ge. G. Samsonidze, S. G. Chou, A. Jorio, G. Dresselhaus, and M. S. Dresselhaus, Phys. Rev. B **72**, 235408 (2005).